Applied Ocean Research 168 (2026) 104972

Contents lists available at ScienceDirect

Applied Ocean Research

journal homepage: www.elsevier.com/locate/apor

Research paper

Spatiotemporal numerical modeling of wave overtopping flow over dike crests and landward slopes

Niels van der Vegt [a,b,*], Bas Hofland [c], Vera M. van Bergeijk [d], Suzanne J.M.H. Hulscher [a], Jord J. Warmink [a]

[a] Department of Civil Engineering and Management, University of Twente, Enschede, The Netherlands
[b] HKV Consultants, Lelystad, The Netherlands
[c] Department of Hydraulic Engineering, Delft University of Technology, Delft, The Netherlands
[d] Department of Coastal Structures and Waves, Deltares, Delft, The Netherlands

ARTICLE INFO

Dataset link: https://github.com/nielsvandervegt/boreflow

Keywords:
Wave overtopping
Numerical modeling
Flow velocity
Flow thickness
Hydraulic loading
Dike crest
Landward slope

ABSTRACT

Wave overtopping can cause severe erosion on the crest and landward slope of a dike. Accurate erosion prediction requires resolving the spatiotemporal evolution of overtopping flow, which remains insufficiently understood. This study investigates the behavior of overtopping flow along the crest and landward slope using a new, efficient numerical model based on the Steep-Slope Shallow Water Equations. The model was validated against measurements from field experiments using a wave overtopping simulator.

The model was applied to a typical dike geometry (B_c = 5 m; $\tan(\alpha)$ = 1V:3H), where the overtopping flow is imposed at the waterside crest line based on a schematization using empirical equations from literature and insights from small-scale overtopping experiments. The spatiotemporal evolution of the flow was analyzed along the crest and landward slope for different overtopping volumes. The flow was observed to stretch in time along both the crest and slope while the wavefront steepens, causing the peak flow thickness (h_{peak}) to decrease significantly. The peak flow velocity (u_{peak}) decreases along the crest but initially accelerates on the slope due to gravitational forcing. As the flow becomes progressively thinner and faster downslope, frictional forcing increases, reducing the acceleration. Eventually, gravitational and frictional forces balance, causing u_{peak} to decelerate and then decrease.

Overall, the model captures key spatiotemporal dynamics such as flow stretching, wavefront steepening, and deceleration of u_{peak} on long slopes, which are absent in time-independent analytical models. It offers a computationally efficient approach that provides a practical middle ground between simplified analytical methods and full CFD simulations.

1. Introduction

Erosion caused by wave overtopping is one of the dominant failure modes for dikes. To protect against this erosion, the crest level and landward slope are carefully designed to prevent breaching under normative storm conditions. Erosion modeling plays a key role in the design process by predicting the expected erosion damage during such events.

For the interaction between overtopping waves and the grass cover on the crest and landward slope, several erosion models have been developed (Hughes and Shaw, 2011; van der Meer et al., 2011; van Bergeijk et al., 2021). These models generally assume that the erosion damage caused by an individual overtopping wave is time-dependent and driven by the extent to which the loading exceeds a critical threshold (Dean et al., 2010). Specifically, both the duration of exceedance and the magnitude of the excess loading contribute to the total erosion damage. To apply these erosion models effectively, it is crucial to know how overtopping flow evolves along the slope and to be able to resolve the spatiotemporal evolution of the flow velocity u and thickness h for any given overtopping volume.

Several studies have examined overtopping flow characteristics along the crest and landward slope. Most of these have focused on peak flow parameters, such as the peak flow velocity (u_{peak}) and peak flow thickness (h_{peak}), defined as the local maxima of velocity and thickness of the overtopping flow at a given position along the crest or slope. A subset of studies developed analytical models (Schüttrumpf and Oumeraci, 2005; van Bergeijk et al., 2019) that estimate u_{peak} from simplified continuity and momentum equations. To obtain analytical solutions, these models assume a constant discharge q at u_{peak} along

* Corresponding author at: Department of Civil Engineering and Management, University of Twente, Enschede, The Netherlands.
E-mail address: N.vanderVegt@utwente.nl (N. van der Vegt).

https://doi.org/10.1016/j.apor.2026.104972
Received 14 October 2025; Received in revised form 16 January 2026; Accepted 9 February 2026
Available online 12 February 2026

the crest and landward slope, neglecting any time-dependent changes in q. This simplification can lead to an overestimation of momentum and thus of u_{peak}, particularly for smaller overtopping volumes (van Bergeijk et al., 2019). The peak flow thickness, h_{peak}, is typically derived from the continuity equation, assuming that u_{peak} and h_{peak} coincide. However, Hughes and Thornton (2016) and Hughes (2017) observed a time lag between u_{peak} and h_{peak}, indicating that this assumption is not always valid. While these analytical models are physics-based and allow rapid estimation of u_{peak}, they offer limited insight into the underlying flow physics and do not resolve the full spatiotemporal evolution of u and h.

Other studies have examined wave overtopping using computational fluid dynamics (CFD) models such as OpenFOAM, DualSPHysics, or SWASH (Gruwez et al., 2020; Altomare et al., 2021; Chen et al., 2021, 2022; van Bergeijk et al., 2022; Schrama et al., 2026). These models can resolve the full spatiotemporal evolution of u and h (van Bergeijk et al., 2022). However, they typically require a deep understanding of CFD, extensive calibration, and several hours of computation time. While once set up, such models can offer opportunities for further insight into the physics of overtopping flows, they are less suitable for quick calculations. For example, to quickly estimate the hydraulic loading needed to predict erosion for a whole range of different overtopping volumes and dike geometries.

The objective of this study is to improve the understanding of wave overtopping flow dynamics along the dike crest and landward slope. The new insights gained in this study help dike engineers to make design choices about the geometry of the crest and landward slope and support the further development of erosion models. Since neither analytical nor CFD models provide a fast and efficient way to obtain the spatiotemporal evolution of flow velocity u and thickness h for arbitrary wave overtopping volumes, this study introduces a numerical model based on the Steep-Slope Shallow Water Equations (SSSWE) (Maranzoni and Tomirotti, 2022). This model enables efficient simulation of the full spatiotemporal evolution of overtopping flows, providing a relatively simple yet effective alternative that overcomes key limitations of existing analytical methods while keeping computation times limited.

The structure of this paper is as follows. Because the proposed model resolves the temporal evolution of the flow, suitable temporal boundary conditions must first be defined. In Section 2, time series of $u(t)$ and $h(t)$ are established at the waterside crest level for a given overtopping volume based on literature. In Section 3, a numerical model based on the Steep-Slope Shallow Water Equations (SSSWE) is developed and validated using data from field experiments. In Section 4, the spatiotemporal behavior of overtopping flow along the crest and landward slope is analyzed for different overtopping volumes, followed by a sensitivity analysis on the dike geometry. The results are discussed and compared with previous studies in Section 5, and the conclusions are presented in Section 6.

2. Temporal schematization of overtopping flow at the waterside crest line

We start by developing a schematization of the overtopping flow at the waterside crest line, which is needed to define the flow at the upstream boundary of the model. Specifically, we focus on how the time-averaged flow velocity $u_0(t)$ and flow thickness $h_0(t)$ evolve and depend on the overtopping volume V_T and waterside slope angle α_w.

Ideally, this would be done with large-scale flume experiments. However, such datasets are rare, and the limited available datasets (e.g. Smith (1994)) lack accurate measurements at the waterside crest line. Therefore, this schematization is developed using empirical models from the literature and an existing dataset of small-scale overtopping experiments. First, we estimate the peak values of flow velocity and thickness ($u_{peak,0}$ and $h_{peak,0}$). Next, we describe how these flow characteristics vary over time to obtain $u_0(t)$ and $h_0(t)$.

2.1. Peak flow characteristics

In literature, two main approaches exist to predict the peak flow velocity ($u_{peak,0}$) and thickness ($h_{peak,0}$) at the waterside crest line. The first relates the individual overtopping volume (V_T) directly to the peak flow characteristics. van der Meer et al. (2011) proposed power-law relationships between V_T, u_{peak}, and h_{peak}, based on measurements from overtopping waves generated by a wave overtopping simulator (WOS). While the WOS is designed to closely simulate real overtopping waves, these relationships remain indirect since they are not directly derived from natural overtopping events. Alternatively, Hughes (2017) derived empirical equations based on overtopping measurements from small-scale tests conducted with deep-water conditions (FlowDike).

The second and more commonly used method relates $u_{peak,0}$ and $h_{peak,0}$ to the run-up exceedance height ($R_u - R_c$), using a simplified energy balance, see Eq. (1) (van der Meer and Klein Breteler, 1991). Here, R_c is the freeboard of the dike, defined as the vertical distance between the still water level and the dike crest. R_u denotes the wave run-up height, defined as the vertical distance between the still water level and the highest point reached by wave run-up on an infinitely long slope. The relation between the peak flow characteristics and the run-up exceedance height has been studied extensively, as 2% exceedance values of wave run-up were long considered standard practice (van Gent, 2002; Schüttrumpf and Oumeraci, 2005; Bosman et al., 2009; van der Meer et al., 2011, 2012; Formentin et al., 2019). The coefficients $c_{u,2\%}$ and $c_{h,2\%}$ in these studies have been calibrated primarily using small-scale experiments and numerical models. All coefficients are included in Appendix B.

$$\begin{aligned} u_{peak,2\%,0} &= c_{u,2\%}\sqrt{g\left(R_{u,2\%} - R_c\right)} \\ h_{peak,2\%,0} &= c_{h,2\%}\left(R_{u,2\%} - R_c\right) \end{aligned} \tag{1}$$

The flow characteristics in Eq. (1) refer to 2% exceedance statistics based on all incoming waves. However, under the assumption that run-up and peak flow characteristics both follow Rayleigh distributions (Battjes, 1974; van der Meer et al., 2012; van Damme, 2016), the equations can also be applied to individual run-up events without modifying $c_{u,2\%}$ (= c_u) and $c_{h,2\%}$ (= c_h).

Next, Eq. (1) can be expressed in terms of the individual overtopping volume V_T. Hofland et al. (2015) demonstrated that the run-up exceedance height ($R_u - R_c$) can be related to the V_T by integrating the surface area of the flow above the crest level. Following this approach, van Damme (2016) proposed Eq. (2). Where f_v is a shape factor (2 for triangular wave shapes) and c_d is the gradient in wave run-up thickness, taken as 0.055 following van Damme (2016).

$$R_u - R_c = \sqrt{\frac{f_v \sin^2(\alpha_w)}{c_d \cos(\alpha_w)} V_T} \tag{2}$$

In Fig. 1, the equations proposed in the various studies are shown by relating V_T to both $u_{peak,0}$ and $h_{peak,0}$. For this comparison, a waterside slope angle of 1V:4H is used, as it is the only slope within the validity range of all equations and a typical slope angle for (sea) dikes. The equations derived from measurements of generated overtopping waves in the WOS van der Meer et al. (2011) are shown as dotted lines, as they cannot be directly compared to the others. For studies that relate peak flow characteristics to the run-up exceedance height ($R_u - R_c$), the conversion to V_T is made by substituting Eq. (2) in Eq. (1). Consequently, almost all equations are now in terms of only the overtopping volume and the waterside slope angle. The only exception is the equation of Hughes (2017) for $u_{peak,0}$, which also requires the spectral wave period ($T_{m-1,0}$). For this equation, a $T_{m-1,0}$ between 4.0 and 7.0 s was assumed, representative of storm conditions.

Fig. 1 shows generally good agreement among the different equations predicting the u_{peak}. A notable exception is the equation by Hughes (2017), which predicts relatively low velocities. The equations

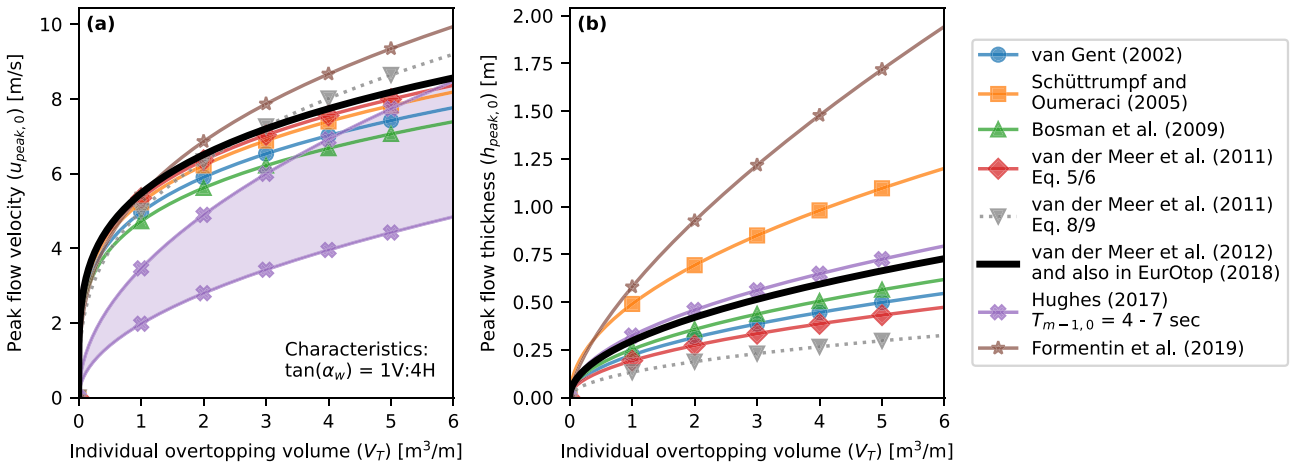

Fig. 1. Comparison between equations proposed in the literature: (a) equations between V_T and $u_{peak,0}$; (b) equations between V_T and $h_{peak,0}$. The equations of van der Meer et al. (2011), shown by the dotted lines, are calibrated on the flow simulated by the wave overtopping simulator.

predicting h_{peak} show larger variation across studies. Notably, the equations proposed by Schüttrumpf and Oumeraci (2005) and Formentin et al. (2019) differ significantly. The discrepancies in Schüttrumpf and Oumeraci (2005) can be attributed to differences in experimental setup and instrumentation (Schüttrumpf and van Gent, 2003; Bosman et al., 2009). The equation by Formentin et al. (2019), which yields relatively high u_{peak} values, is based on non-dimensionless data from small-scale experiments with a maximum $R_{u,2\%} - R_c$ of 0.55 m. Applying this equation to the volumes considered here requires substantial extrapolation, which may explain the differences for large volumes.

Given these observations, the equation by van der Meer et al. (2012) (black line in Fig. 1) is the preferred choice. It is based on a well-established dataset that combines results from multiple experiments (van Gent, 2002; Schüttrumpf and Oumeraci, 2005; Bosman et al., 2009; van der Meer et al., 2011) and is also included in EurOtop (2018). Therefore, this equation is used in the present study to predict $u_{peak,0}$ and $h_{peak,0}$ at the waterside crest line.

2.2. Temporal schematization

The temporal evolution of an overtopping wave at the waterside crest line can be characterized by its duration and shape. We first focus on the duration, quantified by the overtopping time (T_{ovt}), for which we adopt the equation proposed by Hughes (2017), see Eq. (3). This is the only dimensionally consistent formulation, whereas other studies propose purely empirical relations of the form $T = aV^b$ (Bosman et al., 2009; Hughes et al., 2012) or equations specific to the wave overtopping simulator (van der Meer et al., 2011).

$$T_{ovt} = 15.56 \left(\frac{\sqrt{V_T}}{g} \right)^{0.5} \tag{3}$$

Secondly, the evolution shape describes how flow velocity ($u_0(t)$) and flow thickness ($h_0(t)$) change over time within an overtopping wave at the waterside crest line. Bosman et al. (2009) proposed a triangular shape for both $u_0(t)$ and $h_0(t)$, starting at $u_{peak,0}$ and $h_{peak,0}$ at $t = 0$ and decreasing linearly to zero at $t = T_{ovt}$. A limitation of this model is that the integrated discharge $u_0(t) \cdot h_0(t)$ does not necessarily match the overtopping volume V_T. To address this, Hughes and Shaw (2011) introduced exponents a and b, calibrated such that the integrated discharge equals V_T, as shown in Eq. (4). In this study, we adopt the same calibration method while assuming $a = b$, since no studies have investigated whether the temporal evolution of $u_0(t)$ differs from that of $h_0(t)$.

$$\begin{aligned} u(t) &= u_{peak} \left(1 - \frac{t}{T_{ovt}} \right)^a \\ h(t) &= h_{peak} \left(1 - \frac{t}{T_{ovt}} \right)^b \end{aligned} \tag{4}$$

The evolution shapes proposed by Bosman et al. (2009) and Hughes and Shaw (2011) assume that $u_{peak,0}$ and $h_{peak,0}$ occur simultaneously at the wavefront (the moment when the maxima occurs $t_{u_{peak,0}} = t_{h_{peak,0}} = 0$ s). However, Hughes (2015) found that $u_{peak,0}$ and $h_{peak,0}$ often do not coincide in time. No studies have yet examined or quantified this time lag for large-scale wave overtopping. Data from small-scale experiments could be used, but they may not capture the wavefront accurately due to limited sampling frequency or measurement device inertia, such as with micro-propellers. Nevertheless, a time lag needs to be introduced to prevent an infinitely steep wavefront and unrealistic flow development in the numerical model.

Therefore, we make an assumption for $t_{u_{peak,0}}$ and $t_{h_{peak,0}}$. It is known that $u_{peak,0}$ occurs near the wavefront and typically before $h_{peak,0}$ (Hughes and Shaw, 2011). To avoid placing $u_{peak,0}$ at $t = 0$ where $h_0(t) = 0$, we introduce a small time lag and set $t_{u_{peak,0}}$ at 1% of T_{ovt}. Next, we estimate the time lag between $h_{peak,0}$ and $u_{peak,0}$ based on FlowDike experiments for a 1:3 waterside slope (Lorke et al., 2012). In total, we selected 2472 individual overtopping events from the dataset of Hughes and Thornton (2016), all with Reynolds numbers greater than 1000 and Weber numbers greater than 10, to minimize scale effects (Heller, 2011). Since the time lag develops in the wave run-up flow on the waterside slope, where velocities and flow depths are higher than in the subsequent overtopping flow, the governing part of the formation of the time lag occurs at higher local Reynolds and Weber numbers.

In Fig. 2, the time lag of the selected overtopping events at the waterside crest line is shown. We find that $h_{peak,0}$ occurs on average 7% of T_{ovt} after $u_{peak,0}$. Adding this to the 1% of T_{ovt} lag for $t_{u_{peak,0}}$, we find that $t_{h_{peak,0}}$ occurs on average at about 8% of T_{ovt}. This assumption is validated against field experiments with the wave overtopping simulator in Section 3.2.

2.3. Schematization

By combining the relationships of the peak flow characteristics in Section 2.1 with the temporal evolution in Section 2.2, the flow of an overtopping wave at the waterside crest line ($u_0(t)$ and $h_0(t)$) can be schematized in time. This schematization depends on the individual overtopping volume (V_T) and the waterside slope angle (α_w). In Fig. 3, the time series $u(t)$ and $h(t)$ are schematized for three individual overtopping volumes.

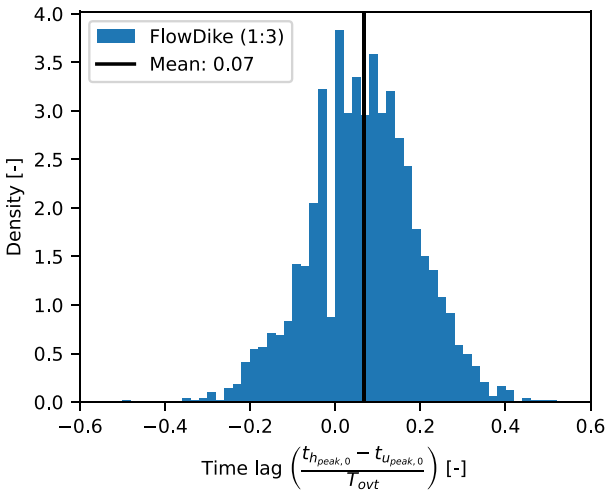

Fig. 2. Time between h_{peak} and u_{peak} expressed as ratio over T_{ovt} from individual overtopping events during the FlowDike experiments with a 1:3 slope (n = 2472).

The figure illustrates that both flow velocity and thickness have steep fronts, with the flow velocity displaying the steepest front. After reaching their respective peaks, they gradually decay back to zero. When the product of $u(t)$ and $h(t)$ is integrated over time, the result is equal to the individual overtopping volume.

3. Modeling overtopping flow over a dike

3.1. Numerical model

Next, we focus on modeling the wave overtopping flow in both space and time. van Bergeijk et al. (2019) used the Shallow Water Equations (SWE) for their analytical model. Their SWE formulation assumes a gently sloped bottom, typically around 1V:10H or milder (Chow, 2009), which allows for the derivation of the analytical solution. However, since the landward slope of a dike is typically much steeper, and we are not constrained by the simplifications required for an analytical solution, we must account for slope effects explicitly. This is achieved by applying the one-dimensional Steep-Slope Shallow Water Equations (SSSWE) in our numerical model (Ancey et al., 2008; Maranzoni and Tomirotti, 2022). The SSSWE is a specialized form of the SWE formulated to accommodate steeper slopes. When applied to a horizontal surface, the SSSWE simplifies to the SWE, making it applicable to both the crest and landward slope. The one-dimensional SSSWE from Maranzoni and Tomirotti (2022) is used in this study and presented in Eq. (5).

$$\begin{aligned} &\frac{\delta h_z}{\delta t} + \frac{\delta(u\, h_z\, \cos(\alpha))}{\delta x} = 0 \\ &\frac{\delta(u\, h_z)}{\delta t} + \frac{\delta}{\delta x}\left[\left(u^2\, h_z + \frac{1}{2}\, \cos^2(\alpha)\, g\, {h_z}^2\right)\cos(\alpha)\right] = \\ &g\, h_z\left(\sin(\alpha) - \frac{n^2\, u^2}{{h_z}^{4/3}}\sqrt{1+\tan^2(\alpha)}\right) \end{aligned} \tag{5}$$

Here, t is time (s), g is the gravitational acceleration (9.81 m/s^2), and n is Manning's coefficient (s/m$^{1/3}$). See Fig. 4 for the definitions of the other parameters. In the remainder of this study, we define the flow thickness perpendicular to the surface, see Eq. (6).

$$h = h_z \cos(\alpha) \tag{6}$$

The SSSWE incorporates the effects of the bottom slope and differs from the SWE in five key aspects (Maranzoni and Tomirotti, 2022). Firstly, the SSSWE employs a different coordinate system, where the depth-averaged flow velocity is modeled parallel to the bottom slope, while the flow thickness is defined vertically, as shown in Fig. 4. Secondly, on steep slopes, the vertical pressure distribution deviates from hydrostatic conditions. The SSSWE accounts for this by introducing a correction factor based on the bottom slope, specifically $\cos(\alpha)^2$. Thirdly, the gravitational term is adjusted by replacing the small-angle approximation with $\sin(\alpha)$ to represent more accurately the influence of steep slopes. Fourthly, the convective acceleration term is modified by a factor of $\cos(\alpha)$, ensuring accurate representation of flow dynamics along the inclined bed. Lastly, the friction term is adapted to consider that, on steep slopes, the actual bottom surface length is larger than its horizontal projection, neglecting this would lead to an underestimation of friction stresses.

3.1.1. Boundary conditions

The physical domain of the dike is modeled from the waterside crest line toward the landward side, for example, up to the toe of the dike, see Fig. 4. The geometry of the dike is modeled by expressing the slope angle as a function of the x-coordinate, $\alpha(x)$. The same is possible for Manning's coefficient $n(x)$, however, transitions between revetments with different roughnesses are outside the scope of this study. A constant Manning's coefficient $n = 0.0175$ is therefore adopted to represent a grass cover, based on wave overtopping field experiments on grass-covered dikes in the Netherlands (van Bergeijk et al., 2020).

The upstream boundary is located at the waterside crest line of the dike, where a time-dependent Dirichlet condition is applied to impose overtopping flow. Here, the flow velocity $u_0(t)$ and flow thickness $h_0(t)$ are determined using the schematization in Section 2, allowing the simulation of any individual overtopping volume. At the downstream end, a free outflow boundary condition is imposed.

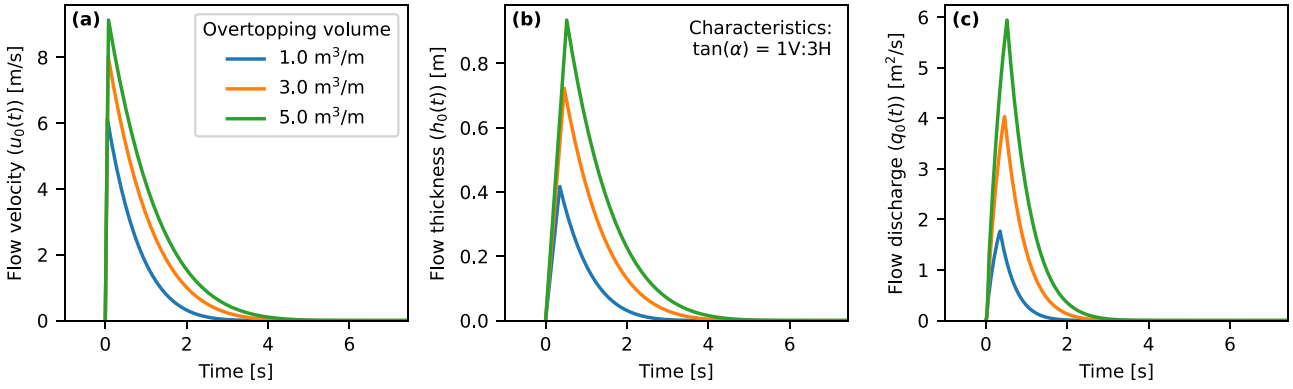

Fig. 3. Schematized temporal evolution of the overtopping wave flow at the waterside crest line for varying overtopping volume: (a) flow velocity $u_0(t)$; (b) flow thickness $h_0(t)$; (c) flow discharge $q_0(t) = u_0(t)\, h_0(t)$.

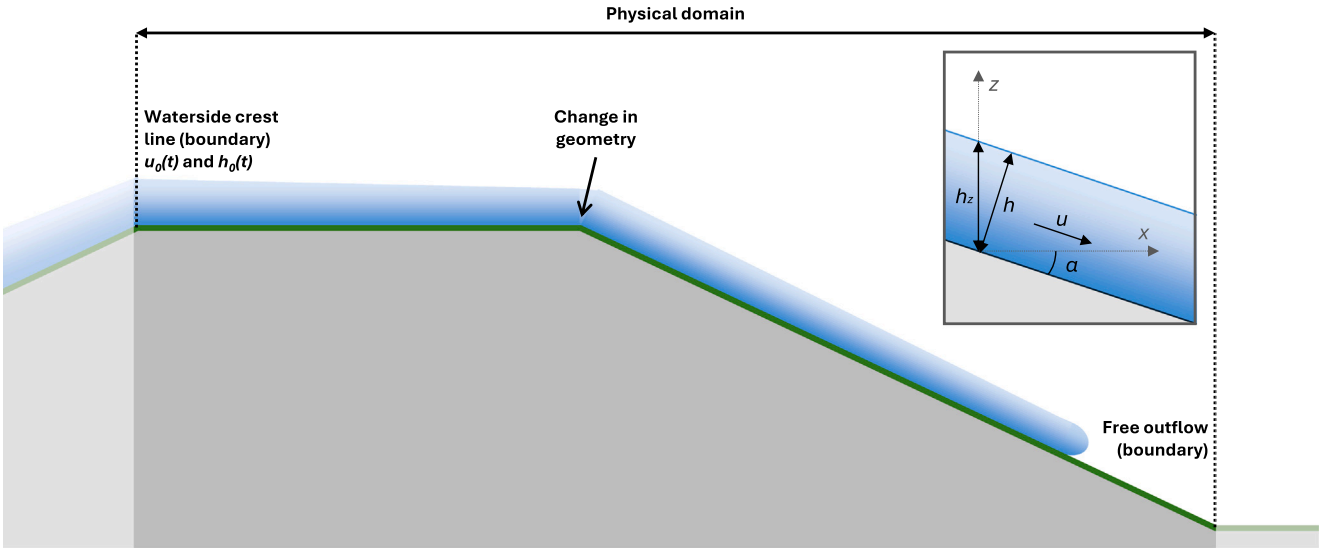

Fig. 4. The Steep-Slope Shallow Water Equation is applied to the crest and landward slope of a dike. Top right: coordinate system used in the Steep-Slope Shallow Water Equations.

3.1.2. Discretization and numerical schemes

The SSSWE are solved numerically using the finite volume method. Specifically, we apply the Monotonic Upstream-centered Scheme for Conservation Laws (MUSCL) by van Leer (1979). The MUSCL scheme is well-suited for modeling shocks and discontinuities (Toro, 2009), making it effective for capturing the wetting wavefront of the overtopping flow. We use the minmod slope limiter (Roe, 1986), as it provides the most stable results near the wavefront and prevents spurious velocity peaks that were observed with less diffusive limiters, such as van Leer and monotonized central (van Leer, 1974, 1977). Time integration is performed using the second-order accurate Runge–Kutta (RK2) method (Runge, 1895; Vuik et al., 2023). The overall scheme is second-order accurate in space and time, but reduces to first-order accuracy in space near extrema and discontinuities, such as the wavefront, due to the application of slope limiters.

The fluxes between the cells are calculated using the Harten–Lax–van Leer (HLL) flux (Harten et al., 1983). The HLL flux is sufficient for modeling overtopping flow, as contact discontinuities are not present. Additionally, the HLL resulted in more stable results than the Rusanov flux (Rusanov, 1961; Toro, 2009) in our tests. The timestep is dynamically adjusted according to the Courant–Friedrichs–Lewy (CFL) condition (Courant et al., 1928), which ensures that the flow does not travel more than one grid cell per time step, thereby maintaining numerical stability. Based on tests, a CFL number of 0.1 combined with a grid spacing of $\Delta x = 0.10$ m provided the best balance between accuracy and computational efficiency.

3.2. Validation using wave overtopping simulator field experiments

To validate the numerical model, we compare its predictions with measurements of overtopping flow at multiple locations along the crest and the landward slope. Similar to the temporal schematization at the waterside crest line (see Section 2), the most ideal is to use large-scale flume experiments. However, the limited available datasets (e.g. Smith (1994)) lack accurate measurements of $u(t)$ and $h(t)$ at multiple locations needed to reconstruct the spatiotemporal evolution of an overtopping wave. Therefore, we use field experiments in which large overtopping flows were generated by the Wave Overtopping Simulator (WOS).

3.2.1. Measurement setup and instrumentation

The results from the numerical model will be compared against measurements from three WOS field experiments: Tholen, Millingen a/d Rijn, and Nijmegen (Future Dikes project) (Bakker et al., 2011, 2013; Daamen et al., 2023). In these field experiments, additional tests were conducted to measure flow characteristics at several locations on the crest and landward slope. The tested cross-section at Millingen a/d Rijn is shown in Fig. 5, while the cross-sections at Tholen and Nijmegen are provided in Appendix C.1.

During the tests, increasingly larger overtopping volumes, ranging from 100 to 5.5 m^3/m, were released from the WOS located on the crest. Each overtopping volume was released and measured two to four times. Instruments were installed at several locations on the crest and landward slope to measure flow velocity ($u(t)$) and/or flow thickness ($h(t)$). Flow velocity was measured using a paddle wheel, and flow thickness was measured perpendicular to the slope using inclined, surfboard-like plates, see Fig. 6. In some cases, the paddle wheel was attached to the surfboard to measure the flow velocity at the free surface (u_{top}), while in other cases it was attached directly to the grass to measure the velocity just above the bed (u_{bot}). Examples of these measurements are shown in Fig. 7.

3.2.2. Numerical model

For each field experiment, the geometry was schematized in the numerical model (red dashed line in Figs. 5, 18 and 20). Although the WOS is designed to closely replicate overtopping flows (van der Meer, 2007), in the initial meters, the boundary layer is not developed yet, so Manning's friction does not apply. Consequently, the schematization from Section 2 cannot be applied directly to the WOS outlet as an upstream boundary. Applying the current schematization there would cause mismatches in u_{peak}, h_{peak}, and T_{ovt} between the model and the measurements, which would result in an unfair comparison down the slope.

To address this, the upstream boundary is shifted to the first measurement location (hatched area in Fig. 5). Using the measurements at this location, new site-specific relations between V_T and u_{peak}, h_{peak}, and T_{ovt} are fitted, see Appendix C.2. The schematization from Section 2 is then adjusted for each field experiment by using the site-specific relations instead of Eq. (1), Eq. (2), and Eq. (3). This ensures that the upstream boundary flow matches the conditions in the field experiments, so that any discrepancies between model results and measurements reflect differences in flow propagation along the slope instead of inconsistencies between the WOS outflow and the schematized boundary condition.

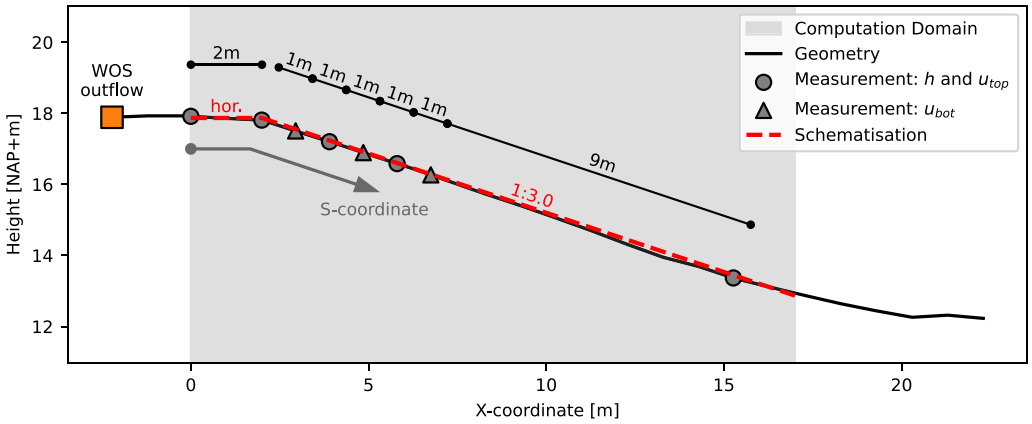

Fig. 5. Geometry of Millingen a/d Rijn from field surveys (black line) (Bakker et al., 2013) and as schematized in the model (red dashed line). The computational domain is shown in gray hatching. Markers indicate measurement locations and types.

Fig. 6. Surfboard-like plate to measure $h(t)$ with a paddle-wheel attached to measure $u(t)$ at the free surface. Photo from Bakker et al. (2013).

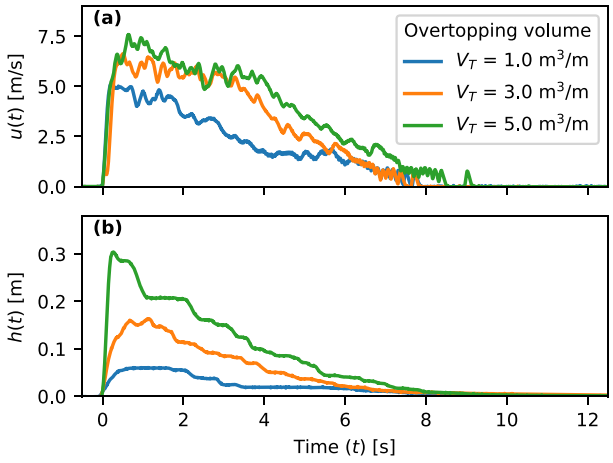

Fig. 7. Example measurements of overtopping flow on the landward slope at Millingen a/d Rijn (s = 6 m from the outflow) for varying released volumes using the wave overtopping simulator (WOS): (a) flow velocity $u(t)$; (b) flow thickness $h(t)$.

3.2.3. Comparison between model results and measurements

We first compare the temporal evolution of $u(t)$ and $h(t)$ between the model and the measurements at several locations along the crest and landward slope. Each measurement location is indicated by its distance from the upstream boundary, which is the first measurement location (s). Figs. 8 and 9 show comparisons for overtopping volumes of 1.5 m^3/m and 4.0 m^3/m at Millingen a/d Rijn. Here, $h(t)$ is defined as the flow thickness normal to the surface for both measurements and model results.

As an additional consistency check, the temporal evolutions of $u(t)$ and $h(t)$ are integrated to approximate the overtopping volume V_T, see Eq. (7). This approach works well for the numerical model, which calculates depth-averaged velocity. In the measurements, velocity is recorded either at the free surface or near the bed. The vertical velocity gradient is, however, estimated to be small (van Hoven et al., 2013), making this a reasonable proxy. This check can also reveal large deviations due to instrumentation errors.

$$V_T = \int_{t=0}^{t=T_{ovt}} h(t)\,u(t)\,dt \tag{7}$$

Figs. 8 and 9 shows at the upstream boundary ($s = 0$ m), $u(t)$ and $h(t)$ are well approximated by the schematization of Section 2, including the derived time lag and site-specific relations for u_{peak}, h_{peak}, and T_{ovt} in Appendix C.2. At downstream locations ($s > 0$ m), the model also reproduces the measured $u(t)$ and $h(t)$ accurately. Both the peak values, the moment that these occur (time lag), and the shapes of the temporal evolutions match closely. The arrival time of the wavefront likewise agrees with the measurements, indicating that the model also provides reliable estimates of the wavefront velocity.

In addition to the temporal evolutions, we will make a full comparison between the peak flow characteristics for all field experiments, released volumes, and available measurement locations. For u_{peak} and h_{peak}, the values are determined based on the maxima of their respective time series. Overtopping time is defined as the duration during which the flow thickness exceeds 2 cm. This threshold was chosen to minimize signal noise. The wavefront arrival time is detected as the first significant increase (> 2 cm) in flow thickness, based on the surfboard signal.

To quantify model performance, we used the Root Mean Square Error (RMSE) and the Nash–Sutcliffe Efficiency (NSE) (Nash and Sutcliffe, 1970). The RMSE provides an absolute measure of the average deviation between model predictions and observations. The NSE evaluates the predictive performance, where a value of 1 indicates perfect agreement, 0 corresponds to performance equal to the mean of the observations, and values below 0 indicate worse performance than the mean.

The comparison in Fig. 10 shows that the model reproduces u_{peak} accurately (RMSE ≈ 0.5–0.6 m/s, NSE ≈ 0.8–0.9). Estimates of h_{peak} are also consistent with the measurements, though with somewhat larger deviations (RMSE ≈ 0.02–0.06 m, NSE ≈ 0.5–0.9). We expect this larger deviation is partly due to the use of the surfboards, which provide a practical solution but is sensitive to splashing, aeration, and the indirect nature of this measurement technique. Two notable outliers

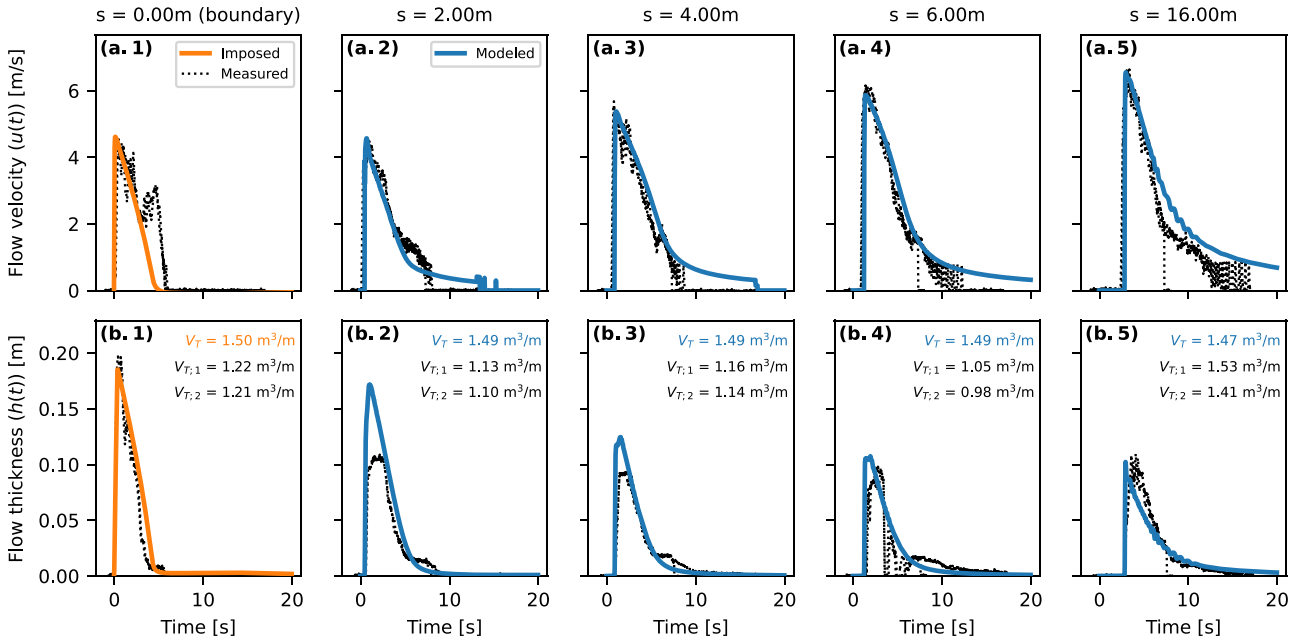

Fig. 8. Comparison between measured and modeled overtopping flow for an overtopping wave with $V_T = 1.5$ m^3/m at Millingen a/d Rijn. Individual measurements are indicated with superscript numbers. Top row (a.1–a.5): flow velocity $u(t)$; bottom row (b.1–b.5): flow thickness $h(t)$. Columns correspond to increasing distance s along the crest and landward slope ($s = 0$, 2, 4, 6, and 16 m).

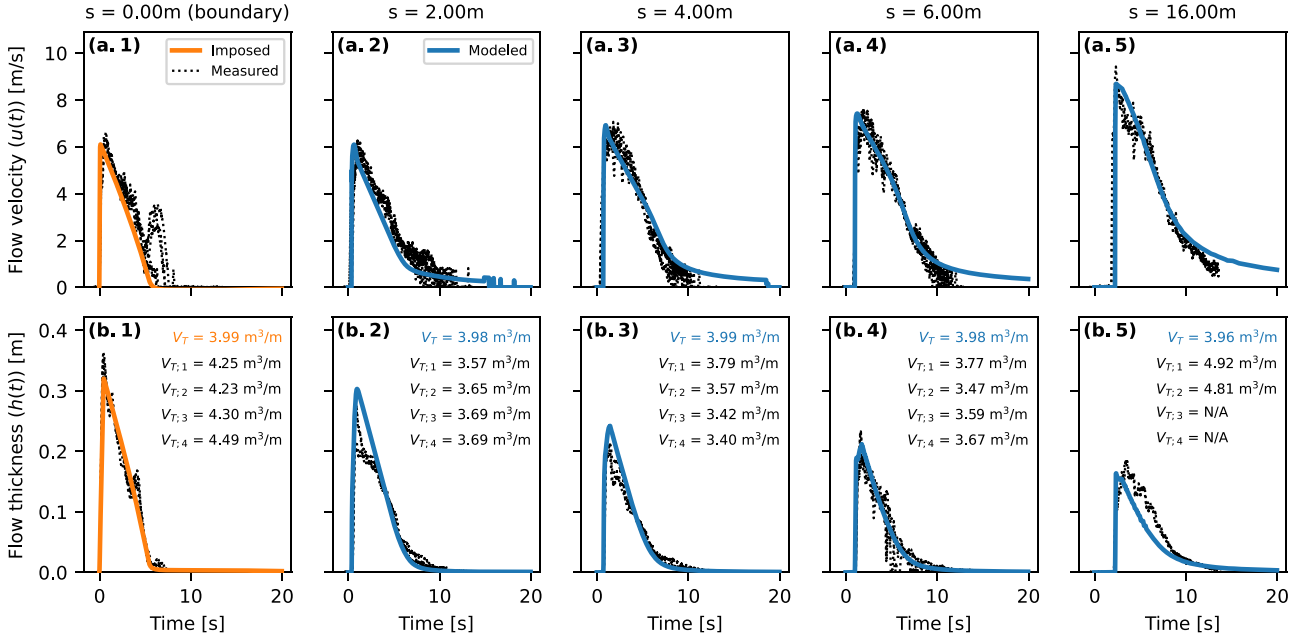

Fig. 9. Comparison between measured and modeled overtopping flow for an overtopping wave with $V_T = 4.0$ m^3/m at Millingen a/d Rijn. Individual measurements are indicated with superscript numbers. Top row (a.1–a.5): flow velocity $u(t)$; bottom row (b.1–b.5): flow thickness $h(t)$. Columns correspond to increasing distance s along the crest and landward slope ($s = 0$, 2, 4, 6, and 16 m). Note that only two measurements are available at s = 16 m, as the other two failed.

were identified: one in Tholen, caused by a measurement spike leading to unrealistically high h_{peak} values (noted by Bakker et al. (2013)), and one in Millingen a/d Rijn, where the surfboard signal at $s = 2$ m appears capped and likely underestimates the true peak (see Appendix C.3). Outside these cases, the agreement between model and measurements is consistent.

The overtopping time T_{ovt} shows somewhat larger deviations. This highlights the difficulty to measure the tail of the wave where the flow thickness is low and thereby the overtopping time. The wavefront arrival time t_{front} is predicted reliably, which indicates the model is also well able to predict the wavefront velocity. Overall, the model provides a realistic description of the spatial and temporal evolution of overtopping flow along the crest and landward slope.

4. Spatiotemporal modeling of overtopping flow

4.1. Model setup

In this analysis, we numerically model and analyze the spatiotemporal flow of overtopping waves along the crest and landward slope. The schematization consists of a dike geometry with a 5-meter-wide crest

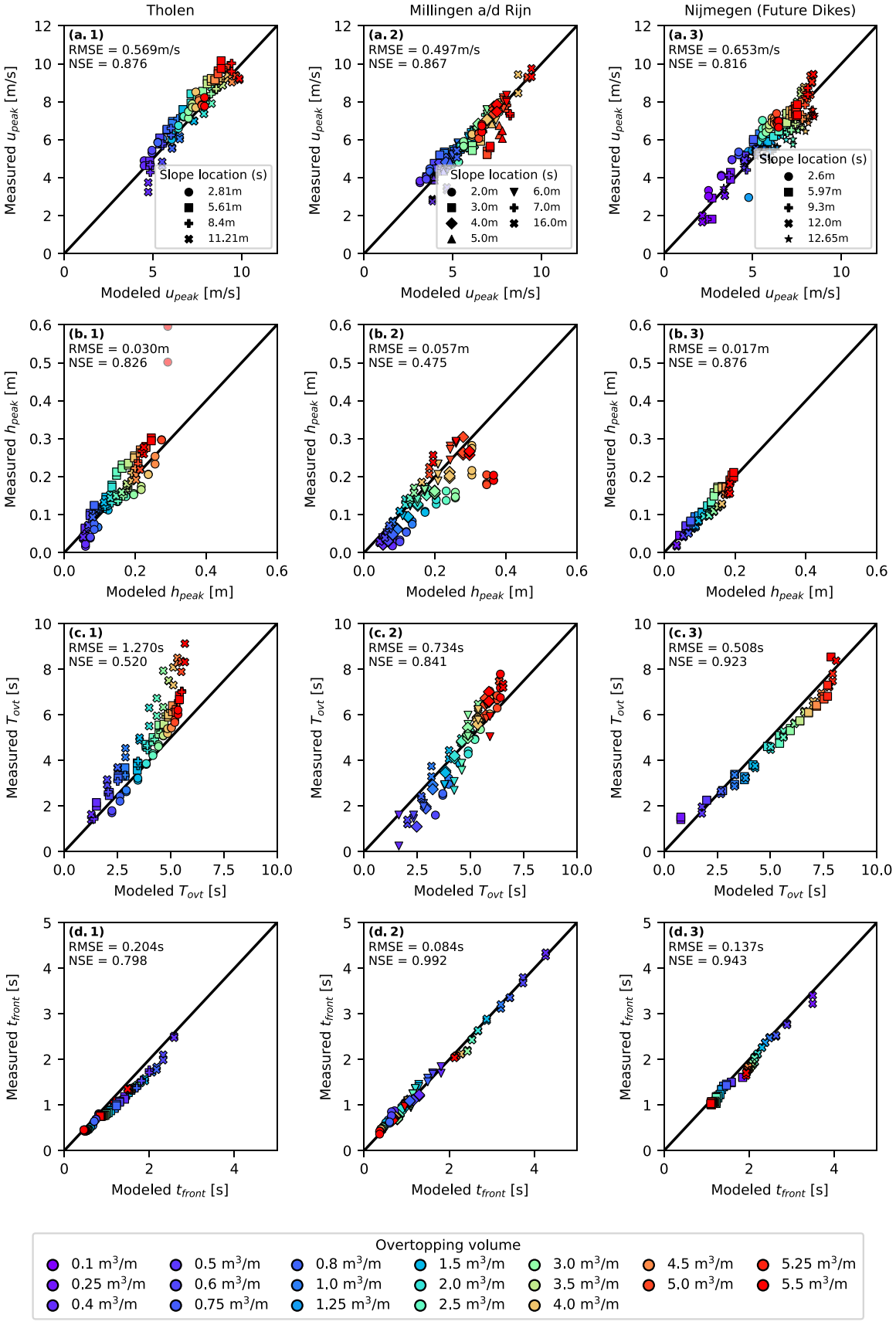

Fig. 10. Comparison between modeled and measured flow characteristics for all measured locations (excluded boundary $s = 0$ m). Columns show the three cases: (a) Tholen, (b) Millingen a/d Rijn, (c) Future Dikes. Rows show the flow characteristics: (1) peak flow velocity u_{peak}; (2) peak flow thickness h_{peak}; (3) overtopping time T_{ovt}; (4) time of wavefront arrival t_{front}. Excluded datapoints are shown transparently.

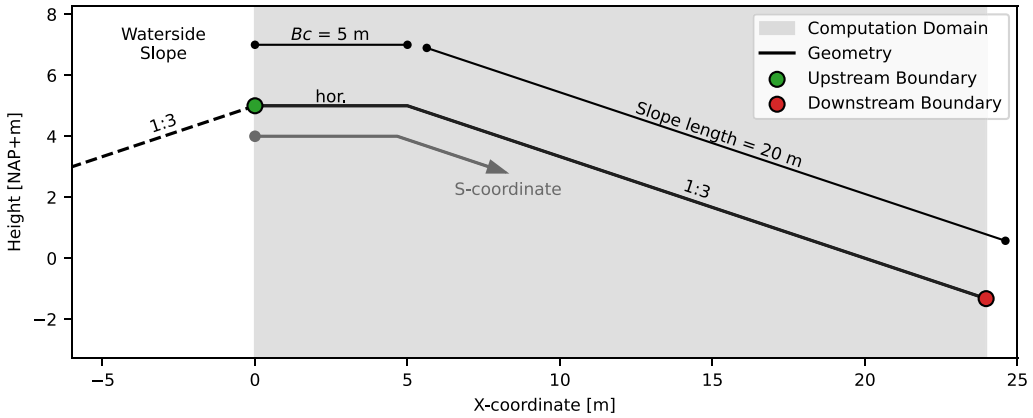

Fig. 11. Dike geometry used in the numerical model (B_c = 5 m; Slope length = 25 m; $\tan(\alpha)$ = 1V:3H; n = 0.0175).

(B_c) and a 20-meter-long landward slope with angle 1V:3H (α), see Fig. 11. Surface roughness is taken as $n = 0.0175$, a value derived from wave overtopping field experiments on grass covers by van Bergeijk et al. (2020).

The upstream boundary is placed at the waterside crest line. Overtopping flow is imposed at this boundary using the schematization of Section 2. Within this schematization, the waterside slope angle must be defined, which is taken here as 1V:3H. For the numerical model, we use the same calculation settings and discretization as in Section 3.

We study the spatiotemporal evolution $u(x,t)$ and $h(x,t)$ for three overtopping volumes (V_T): 1.0 m^3/m (small), 3.0 m^3/m (medium), and 5.0 m^3/m (large). For each volume, we obtain the spatial evolution of the peak flow velocity (u_{peak}), peak flow thickness (h_{peak}), peak flow discharge (q_{peak}), and overtopping time (T_{ovt}) along the landward slope.

For small overtopping volumes on steep landward slopes, spurious oscillations occur near the end of the overtopping flow tail. Likely caused by the high-order MUSCL reconstruction, these oscillations can hinder the accurate determination of T_{ovt}. To mitigate this, a second-order Savitzky–Golay filter is applied to the tail of the flow before determining T_{ovt}.

4.2. Results

Fig. 12 shows the spatial evolution of the peak flow velocity (u_{peak}), peak flow thickness (h_{peak}), peak flow discharge (q_{peak}), and overtopping time (T_{ovt}) along the crest and landward slope for different overtopping volumes.

4.2.1. Overtopping flow on the crest

On the 5-meter-wide crests, the results show that u_{peak} decreases by only about 10% for all overtopping volumes. In contrast, h_{peak} decreases much more strongly, by 50%–60%, with smaller volumes showing the largest relative reduction. Since q_{peak} depends on both u_{peak} and h_{peak}, its trend largely mirrors that of h_{peak}. The overtopping duration T_{ovt} increases by 50%–80%, with larger volumes producing the greater increase. We also observe wavefront steepening, with h_{peak} progressively shifting toward u_{peak}. When both peaks coincide, the product of u_{peak} and h_{peak} equals q_{peak}. This is demonstrated in the bottom left figure of Fig. 12, as it shows that $u_{peak} \cdot h_{peak}$ and q_{peak} converge as the flow travels along the crest.

The decrease in h_{peak} and increase in T_{ovt} can be explained by the changes in flow velocity within the overtopping flow. As the wavefront has a higher flow velocity than the tail, the flow stretches in time along the crest. This causes T_{ovt} to increase, and due to mass conservation, h_{peak} to decrease. The longer the flow gets, the less h_{peak} has to reduce to satisfy this mass balance, which empirically follows an exponential decay trend. The small reduction in u_{peak} occurs because, in the momentum balance near the wavefront, the frictional forcing is much smaller than the convective acceleration forcing. As a result, most of the flow velocity is retained over the crest. The steepening of the wavefront occurs because the thicker flow near h_{peak} retains more momentum and experiences lower frictional resistance. In contrast, the thinner flow near u_{peak} is more strongly affected by friction, causing h_{peak} and u_{peak} to converge, with the time lag between them eventually decreasing to zero.

4.2.2. Overtopping flow on the landward slope

After passing the crest, the flow enters the landward slope. For all overtopping volumes, u_{peak} increases by up to 40% relative to the landward crest line. The strongest acceleration occurs near the top of the slope, while further downslope the acceleration diminishes. Eventually, the flow may start to decelerate as observed for the lowest volume in Fig. 12 ($V_T = 1000$). At the same time, h_{peak} decreases rapidly in the first few meters of the slope (by about 30%), followed by a more gradual reduction further downslope. A comparison between q_{peak} and $u_{peak} \cdot h_{peak}$ indicates further steepening of the wavefront. Finally, T_{ovt} decreases sharply by up to 50% near the top of the slope. After this initial reduction, it increases again for the larger volumes, whereas for the smaller volumes it continues to decrease along the slope.

As the flow enters the slope, it accelerates due to gravity, causing the flow velocity to increase over the entire flow. The difference in flow velocity between the wavefront and tail of the flow increases since the gravitational forcing is proportional to h (see Eq. (5)). This results in the flow to stretch more and h_{peak} to decrease even faster due to mass conservation. This stretching is initially not reflected in T_{ovt}. T_{ovt} decreases in the first few meters as the flow passes more quickly because the flow velocity is higher over the entire flow. As the flow continues to stretch in time along the slope, T_{ovt} starts to increase for larger volumes. For the lowest volume, T_{ovt} further decreases along the slope. This is because the definition for T_{ovt} of $h > 5$ cm is close to h_{peak}, leaving only a diminishing fraction of the overtopping flow above this threshold.

As the overtopping flow progresses along the slope, flow acceleration diminishes. This occurs because faster, thinner flow experiences stronger frictional resistance, as the Manning friction term scales with $u^2/h^{1/3}$ (see Eq. (5)). At a certain point, the frictional forcing balances the gravitational forcing, after which the quasi-uniform velocity decreases together with the decreasing flow thickness, consistent with the Gauckler–Manning equation (Manning, 1891) (see Eq. (8)). This explains why both u_{peak} and h_{peak} decrease beyond this point, and is illustrated by the dash-dotted line for V_T = 1.0 m^3/m in Fig. 12 and

$$u = \frac{1}{n} h^{2/3} \sqrt{\tan(\alpha)} \tag{8}$$

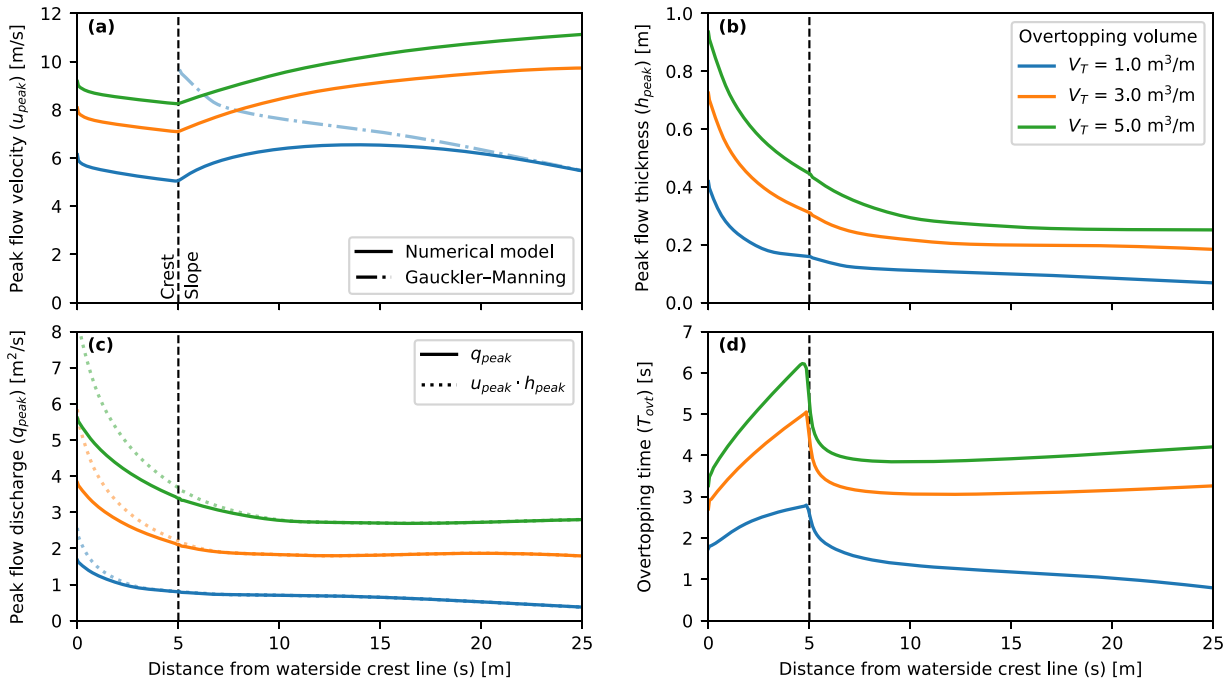

Fig. 12. Spatial evolution of overtopping flow characteristics from the waterside crest line over the dike crest (B_c = 5 m) and landward slope ($\tan(\alpha)$ = 1V:3H): (a) peak flow velocity u_{peak}; (b) peak flow thickness h_{peak}; (c) peak flow discharge q_{peak}, with the dashed line being the product of the u_{peak} and h_{peak}, illustrating the maximum q_{peak} that would occur if both peak values coincided; (d) overtopping duration T_{ovt}. Different overtopping volumes (V_T) are indicated by color.

4.3. Sensitivity analysis

The surface roughness and waterside slope angle are further explored in a sensitivity analysis for 1.0 m^3/m (small) and 5.0 m^3/m (large) overtopping volumes, with 3.0 m^3/m omitted to reduce visual complexity in the graph. For surface roughness, we study a rougher (n = 0.0250) and smoother surface (n = 0.0100). For the waterside slope angle, we study a geometry with a steeper 1V:2H and a gentler 1V:5H landward slope angle.

4.3.1. Surface roughness

Fig. 13 shows the results of a sensitivity analysis for a smoother (n = 0.010) and rougher (n = 0.025) surface roughness along the crest and landward slope. A smoother surface yields higher u_{peak} and shorter T_{ovt} along both the crest and the landward slope. At the same time, h_{peak} is slightly lower for smoother surfaces, with q_{peak} following the same trend. A smoother surface also results in slower steepening of the wavefront, whereas for rougher surfaces the opposite behavior is observed. The influence of roughness is more pronounced for smaller overtopping volumes, as thinner flows are more strongly affected by friction.

$$F_{friction} \propto g \frac{n^2 u^2}{h^{1/3}} \sqrt{1 + \tan^2(\alpha)} \tag{9}$$

By changing the surface roughness, the frictional forcing ($F_{friction}$) in the momentum balance is modified, as shown in Eq. (9) (from Eq. (5)). A smoother surface leads to reduced frictional forcing, which explains the smaller decay in u_{peak} along the crest and slope. This also causes the flow to accelerate over a longer distance on the slope, resulting in the point at which the gravitational and frictional forces are in balance being located further downslope. Because flow velocities are higher throughout the entire flow, T_{ovt} becomes shorter. The higher velocities also increase the difference between the flow velocity near the wavefront and the tail, causing the overtopping wave on smoother surfaces to stretch (slightly) more in time. From mass conservation, this longer flow duration results in a lower h_{peak}. The slower steepening of the wavefront follows from the lower frictional forcing near the wavefront, which decreases the difference in momentum between the region of u_{peak} and h_{peak}, delaying their convergence. For rougher surfaces, the opposite behavior is observed: higher friction produces lower velocities, shorter acceleration lengths, longer overtopping durations, and faster steepening of the wavefront.

4.3.2. Landward slope angle

Fig. 14 shows the results of the sensitivity analysis for a steeper (1V:2H) and a gentler (1V:5H) landward slope. A steeper slope yields higher u_{peak} values, with a stronger initial acceleration near the top of the slope. At the same time, T_{ovt} shows a small reduction for steeper slopes. In contrast, h_{peak} and q_{peak} remain nearly identical between the slopes, and the steepening of the wavefront appears largely unaffected by the slope angle.

$$F_{gravity} \propto g\, h \sin(\alpha) \tag{10}$$

The observed differences in u_{peak} can primarily be explained by the influence of gravitational forcing along the slope, which scales with $\sin(\alpha)$, see Eq. (10)). For steeper slopes, the component of gravity ($F_{gravity}$) acting in the flow direction increases, resulting in stronger acceleration near the top of the landward slope and therefore higher u_{peak} values. At the same time, the frictional forcing also becomes larger for steeper slopes, as shown in Eq. (9), since it scales with the slope angle. These opposing effects partly compensate for each other, explaining why h_{peak} and q_{peak} remain nearly constant between slope angles. The slightly shorter T_{ovt} for steeper slopes results from the higher flow velocities throughout the entire flow, which reduce the time required for the overtopping flow to pass a given location. For gentler slopes, gravitational forcing is weaker, so the flow accelerates less, leading to slightly lower velocities and a longer T_{ovt}, while h_{peak} and q_{peak} remain largely unchanged.

5. Discussion

5.1. Comparison with previous studies

The flow of overtopping waves along the crest and landward slope of a dike has been the subject of numerous previous studies. In the

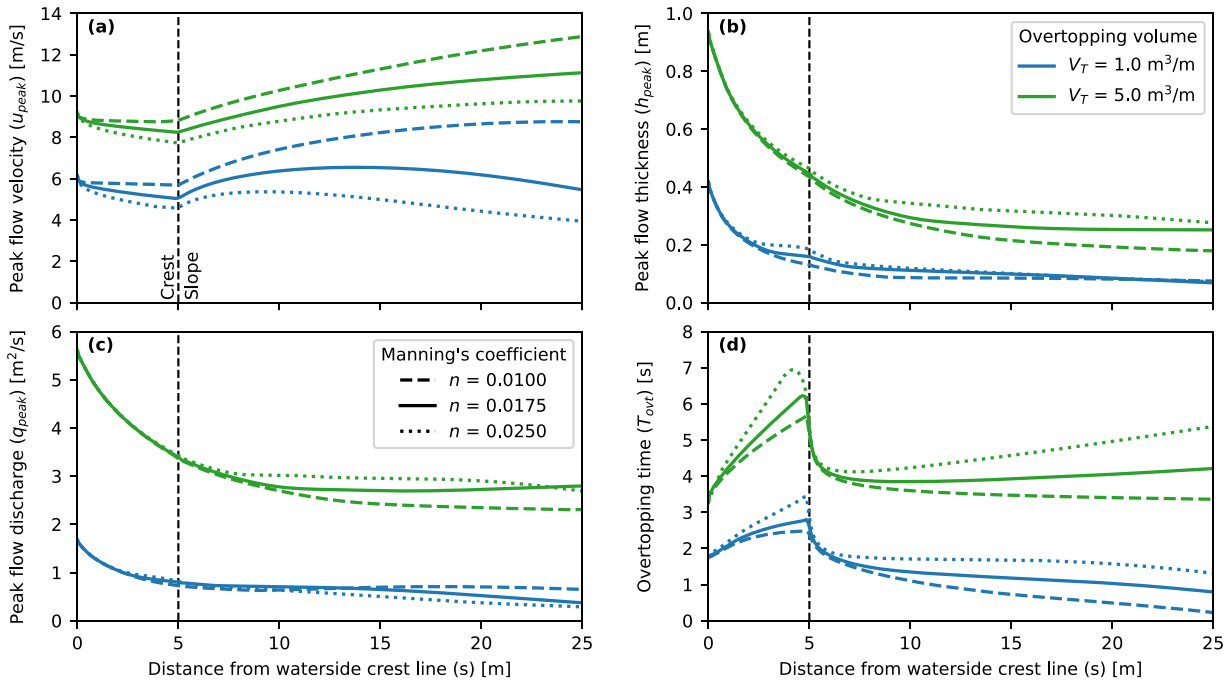

Fig. 13. Spatial evolution of overtopping flow characteristics from the waterside crest line over the dike crest (B_c = 5 m) and landward slope ($\tan(\alpha)$ = 1V:3H): (a) peak flow velocity u_{peak}; (b) peak flow thickness h_{peak}; (c) peak flow discharge q_{peak}; (d) overtopping duration T_{ovt}. Different overtopping volumes (V_T) are indicated by color, and different surface roughnesses (Manning's coefficients n) by line style.

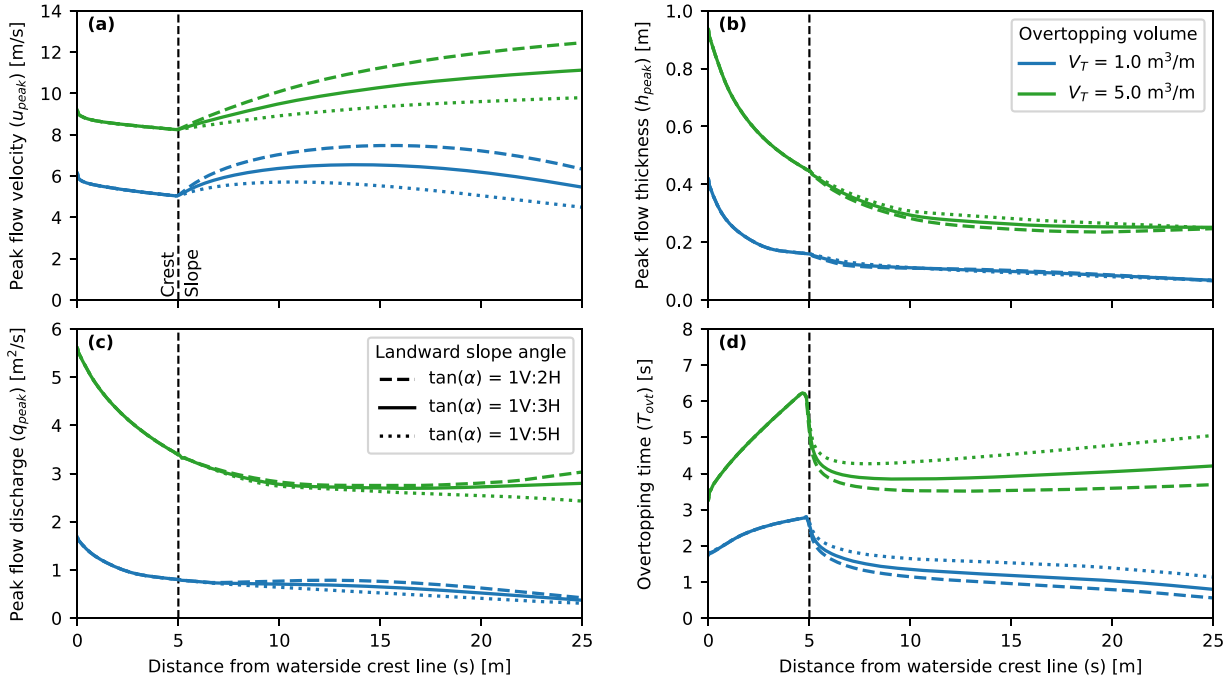

Fig. 14. Spatial evolution of overtopping flow characteristics from the waterside crest line over the dike crest (B_c = 5 m) varying landward slopes: (a) peak flow velocity u_{peak}; (b) peak flow thickness h_{peak}; (c) peak flow discharge q_{peak}; (d) overtopping duration T_{ovt}. Different overtopping volumes (V_T) are indicated by color, and different landward slope angles ($\tan(\alpha)$) by line style.

following two sections, we will compare our findings with those of these studies.

5.1.1. Overtopping flow along the crest

Our analysis in Section 4 showed that the modeled h_{peak} and u_{peak} decrease along the crest, suggesting that the crest width (B_c) influences the extent of this reduction. Moreover, the results revealed clear influences of the overtopping volume (V_T) and surface roughness (n). This general trend of decreasing h_{peak} and u_{peak} along the crest is consistent with previous studies, although reported magnitudes vary (van Gent, 2002; Schüttrumpf and Oumeraci, 2005; Bosman et al., 2009; van der Meer et al., 2011; Guo et al., 2014; Formentin et al., 2019; van Bergeijk et al., 2019).

The studies of Schüttrumpf and Oumeraci (2005) and van Bergeijk et al. (2019) propose analytical equations to model overtopping flow

along the crest. Schüttrumpf and Oumeraci (2005) derived their equation for u_{peak} from the 2D continuity and momentum equations, and proposed an empirical exponential decay for h_{peak} based on measurements, suggesting a constant 53% reduction independent of B_c, V_T, or n. Their approach assumes u_{peak} and h_{peak} occur simultaneously, using h_{peak} as input for u_{peak}. As a result, their model yields larger q_{peak} and slightly higher u_{peak} than the numerical model, which accounts for a time lag between u_{peak} and h_{peak} (see Fig. 15).

van Bergeijk et al. (2019) proposed an analytical model for u_{peak} based on the steady 1D shallow water equations assuming continuity of discharge q at u_{peak}. While no direct equation for h_{peak} was given, they suggested using the discharge continuity to estimate h at u_{peak}. In Fig. 15, we applied this model by defining the momentary discharge as q_{peak} as an approximation for q at u_{peak}. The resulting u_{peak} from the analytical model is higher than in the numerical model. This difference arises because, in the numerical model, q_{peak} (and q in general) varies along the crest, whereas the analytical model is time-independent and assumes it is constant. The numerical model shows q_{peak} decreases along the crest (see also Fig. 12), causing the analytical model to predict a higher u_{peak}. Ultimately, both models depend on an accurate description of the overtopping flow at the waterside crest line, which is discussed further in Section 5.3.

Other studies empirically relate changes in flow characteristics to wave conditions at the dike toe, making direct comparisons less meaningful. For example, van Gent (2002) found u_{peak} to depend on B_c/H_s, and for h_{peak} a constant 33% reduction independent of B_c, V_T, or n (see Fig. 15). Bosman et al. (2009) and van der Meer et al. (2011) proposed exponential decays dependent on B_c and the deep-water (spectral) wavelength. Except for van Gent (2002), the models describe the decay using exponential trends, consistent with our results. In the numerical model, the influence of the wave conditions and waterside slope is not represented explicitly in the boundary conditions defined in Section 2, except for the waterside slope angle (α_w).

Guo et al. (2014) and Formentin et al. (2019) performed more qualitative assessments. Guo et al. (2014) used a two-phase model and found a 50%–60% decay in h_{peak} over a 6-meter-wide crest, but observed an increase in u_{peak}. This may be attributed to the use of a smooth slope, while our simulations used roughness typical of grass. In our sensitivity analysis, we observe almost no decrease of u_{peak} on a smooth crest surface (see Fig. 13). Formentin et al. (2019), using small-scale experiments and mono-phase simulations, reported a 25%–30% linear decrease in h_{peak} and up to 10% decrease in u_{peak}, with an increase of u_{peak} near the landward crest for low freeboard. Their use of a smooth surface and relatively narrow crest (B_c = 15-30 cm) may explain the difference. Additionally, for small freeboards, wave breaking may occur close to the crest. In that case, the flow at the waterside crest line may differ from when breaking occurs lower on the slope.

5.1.2. Overtopping flow along the landward slope

Few studies address the modeling of overtopping flow along the landward slope. In the literature, only van Gent (2002), Schüttrumpf and Oumeraci (2005), and van Bergeijk et al. (2019) present models for this purpose. In Fig. 16, these models are compared with the numerical model from this study. For a consistent comparison, the analytical models were supplied with boundary conditions taken from the landward crest line using the numerical model.

Schüttrumpf and Oumeraci (2005) proposed an iterative analytical equation for u_{peak} on the landward slope based on the steady 2D continuity and momentum equations. Similarly, van Gent (2002) developed an analytical expression for u_{peak} using the steady 1D shallow water equations, which was later refined and validated by van Bergeijk et al. (2019). Both approaches assume continuity of discharge q at u_{peak} along the landward slope, similar to their models of flow over the crest. In Section 4.2.1, we observed that u_{peak} and h_{peak} converge over the crest, implying that q at u_{peak} can be approximated by the product of u_{peak} and h_{peak} at the top of the landward slope, as applied in Fig. 16.

Overall, u_{peak} from the analytical equations agrees well with the numerical model at the top of the slope. However, a key difference is that both analytical models assume constant discharge, while the numerical model shows discharge decreases along the slope (see Fig. 12). This leads to a larger reduction in h_{peak} in the numerical results than in the analytical equations. Additionally, the overestimation of discharge causes the analytical models to overpredict momentum and gravitational forcing (due to overpredicting h) and underpredict frictional forcing. For larger volumes and short slopes, the effect on u_{peak} is small, producing only a slight increase compared to the numerical model. For smaller volumes or long slopes, however, the analytical models predict continued acceleration of the flow, whereas the numerical model shows deceleration once frictional forcing balances the gravitational forcing (see Section 4.2.2). This deceleration has also been observed in field experiments with the WOS, for example, at Tholen and Singapore (Bakker et al., 2011; van der Meer et al., 2020), and was acknowledged as a limitation of the analytical model by van Bergeijk et al. (2019). Such deceleration should be considered when modeling erosion at dikes loaded by relatively low waves, to avoid overestimating the hydraulic loading. This is further elaborated in Section 5.4.

5.1.3. Main differences

Overall, the trends observed in the numerical model, namely the decay of h_{peak} and u_{peak} along the crest and the increase in u_{peak} and decay of h_{peak} along the landward slope, are consistent with previous studies. However, several systematic differences exist. Most analytical or empirical models assume steady flow with constant discharge at u_{peak}, neglecting time-dependent interactions such as the steepening of the wavefront and the stretching of the overtopping flow. In contrast, the numerical model resolves the full spatiotemporal evolution of overtopping flow, revealing new behaviors not captured by previous approaches but observed during field experiments, such as the deceleration of u_{peak} on a long slope. Furthermore, it explicitly accounts for the influence of crest width (B_c), overtopping volume (V_T), and surface roughness (n), representing both the crest and landward slope within a single geometry. This approach features that are often simplified or omitted in analytical or empirical models. Although empirical and analytical models are computationally fast, the numerical model remains relatively quick, with typical calculation times below 10 s depending on geometry and flow, providing a practical middle ground between analytical approaches and full CFD simulations.

5.2. Comparison with other numerical models

Previous studies have applied (non-hydrostatic) shallow water models to simulate wave overtopping. A commonly used model in this category is SWASH, which is a non-linear shallow water solver with pressure correction for the vertical acceleration. SWASH is particularly suited for resolving non-linear wave propagation, breaking, and processes leading up to overtopping (Zijlema et al., 2011). It has been shown to accurately reproduce both average and instantaneous overtopping discharges at the waterside crest line (Suzuki et al., 2017; Gruwez et al., 2020; Ibrahim and Baldock, 2021). While SWASH is in principle capable of simulating overtopping flow on the crest and landward slope, earlier studies have primarily focused on wave run-up and overtopping at the waterside crest.

In the present study, the focus is not on the processes leading up to wave overtopping but on the propagation of individual overtopping flows along the crest and steep landward slope, where the flow is thin, transient, and supercritical. Hence, the Steep-Slope Shallow Water Equations (SSSWE) are applied, as they explicitly account for steep-slope effects through a slope-aligned momentum formulation and modified gravity, pressure, and friction terms (see Section 3.1). By applying the SSSWE, the model is computationally efficient and straightforward to configure for studying this specific flow regime, whereas

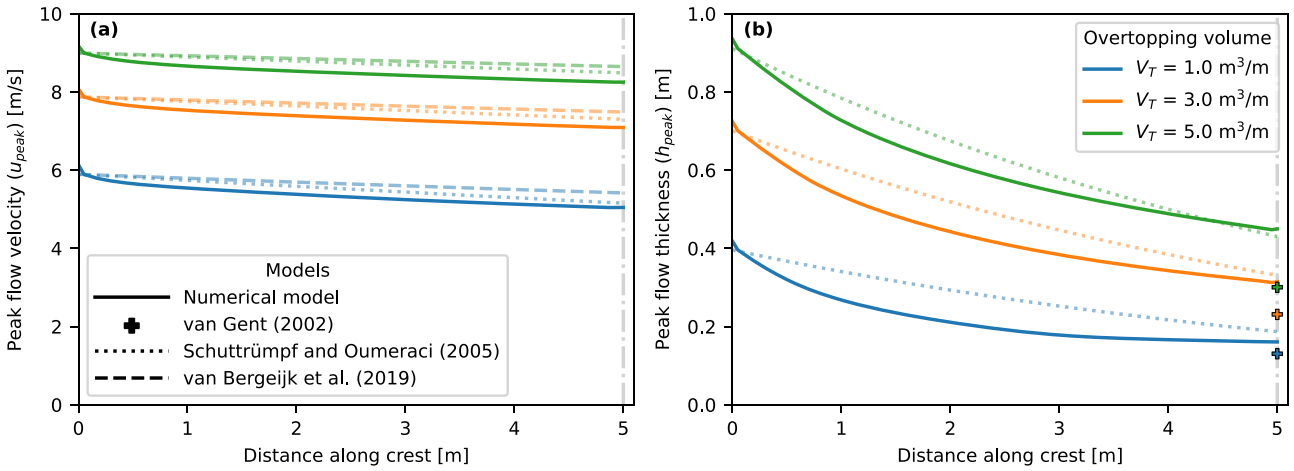

Fig. 15. Comparison of the predicted decay of overtopping flow characteristics on the crest: (a) peak flow velocity u_{peak}; (b) peak flow thickness h_{peak}. Results from the numerical model are compared with analytical models from previous studies.

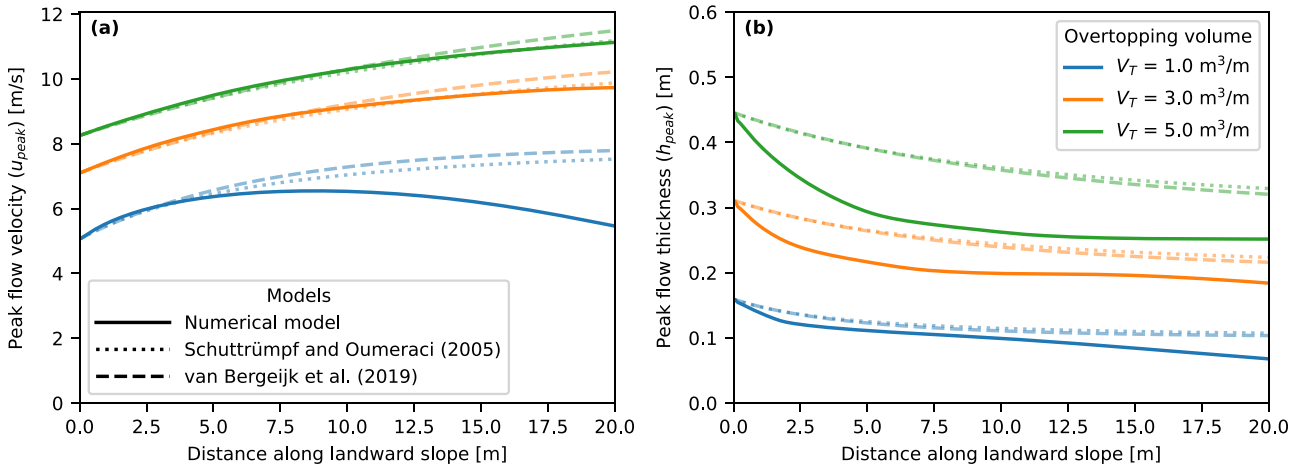

Fig. 16. Comparison of the predicted decay of overtopping flow characteristics on a 1V:3H landward slope: (a) peak flow velocity u_{peak}; (b) peak flow thickness h_{peak}. Results from the numerical model are compared with analytical models from previous studies.

SWASH's numerical framework is designed to resolve a broader range of wave processes than required for the present analysis. This makes the SSSWE-based model well-suited for parametric studies and for use in probabilistic design. Additionally, the SSSWE-based model provides access to the individual terms in the governing equations, allowing the relative contributions of the different forcing terms to be analyzed.

Another option is to use three-dimensional CFD models employing volume-of-fluid (VOF) methods to resolve the free surface, for example, using OpenFOAM® (Jasak, 2009). The main benefit is that these types of models can resolve detailed flow properties such as pressure and near-bed stresses. Previous studies have demonstrated that a two-dimensional OpenFOAM model can accurately reproduce overtopping flow along the crest and landward slope when carefully calibrated against experimental data (Chen et al., 2021; van Bergeijk et al., 2020). However, such models are more complex in setup and calibration, and have high computational cost, which limits their applicability for rapid assessment or studies involving many different overtopping events and geometries. Despite the computational effort required, the models applied in these studies have the same physical limitations as the other models, like neglecting the aeration of the water and not resolving the turbulence.

In conclusion, the SSSWE-based model complements existing numerical models with a targeted and computationally efficient alternative for resolving the spatiotemporal evolution of overtopping flow on crests and steep landward slopes.

5.3. Limitations of the numerical model

The numerical model developed in this study can simulate the overtopping flow along the crest and landward slope of a dike. Based on Section 3.2, we concluded that the model accurately predicts the spatiotemporal evolution of overtopping flow, provided that the upstream boundary condition is well defined. In Section 5.1, we observed that the model aligns with results from partly validated analytical models and improves upon them by addressing some of their limitations.

The main limitation of this study is the definition of the upstream boundary condition, represented by the schematization of the overtopping flow at the waterside crest line. For reproducing the overtopping simulator experiments in Section 3.2, the boundary was placed at the first measurement location, allowing the derivation of well-defined relations between u_{peak}, h_{peak}, T_{ovt}, and the overtopping volume (see Fig. 21). This was possible because the wave overtopping simulator (WOS) produces reproducible flows when releasing the same volume multiple times. In this study, however, we aimed to take a step toward a more general schematization of real overtopping flow at the waterside crest line, rather than relying solely on WOS measurements.

This turned out to be challenging as existing studies show large differences in the proposed relations between u_{peak}, h_{peak}, T_{ovt}, and overtopping volume (Fig. 1). Moreover, the same overtopping volume can lead to significantly different u_{peak} and h_{peak} values, which are

typically negatively correlated (van der Vegt et al., 2025). Nevertheless, we managed in Section 2 to combine most available studies to construct a fair schematization of overtopping flow at the seaward crest line. This schematization performed qualitatively well in Section 4 and in comparisons with other studies in Section 5.1, where the observed results and trends were consistent with the literature.

This study provides a complete and scalable temporal schematization of the overtopping flow at the waterside crest (see Section 2). However, we highly recommend further investigating the full temporal evolution of overtopping waves at the waterside crest line on an individual event basis by conducting measurements during large-scale flume experiments. Primarily because newer erosion models start to rely more on the temporal evolution of individual events (Dean et al., 2010; van der Meer et al., 2011; Hughes and Shaw, 2011; van Bergeijk et al., 2021) but also because previous studies mainly focused only on the 2% quantiles instead of individual events. Data on the waterside crest line from large-scale wave overtopping events are particularly valuable for this purpose, as most studies (see Section 2) rely on small-scale experiments and numerical modeling. Large-scale data would allow to further refine and validate the current schematization.

The second limitation concerns transitions on the crest and landward slope. Geometrical transitions are changes in slope, such as the transition between the crest and landward slope. Due to the abrupt change in slope, energy is expected to dissipate through turbulence. The magnitude of this dissipation, and whether it significantly affects the flow, is currently unknown. In the present model, this additional dissipation is neglected, basically resulting in an upper-bound estimate of the hydraulic loading. For very steep transitions, the flow may even detach for larger overtopping volumes (Ponsioen et al., 2019; van Bergeijk et al., 2022). Such detachment cannot be represented with the SSSWE and would require a two-phase model, such as OpenFOAM (van Bergeijk et al., 2022).

Furthermore, non-geometrical transitions, such as between a grass cover and an asphalt road, can only be partially modeled. Although not validated, the current model supports abrupt changes in roughness but not abrupt changes in height, for example, when the asphalt road is a few centimeters above the grass cover. Introducing such height steps could lead to reflected bores and numerical instabilities, which are not handled in the present implementation. Addressing this would require alternative numerical techniques, such as hydrostatic reconstruction (Audusse et al., 2004) and the use of an appropriate approximate Riemann solver for discontinuities, such as the Harten–Lax–van Leer–Einfeldt (HLLE) scheme (Delis, 2002).

5.4. Practical application

Erosion models for wave overtopping require flow characteristics of the overtopping flow at different locations along the crest and landward slope. The numerical model developed in this study provides these characteristics and can be used to improve erosion modeling. As an example, we demonstrate how the numerical model can help by applying the cumulative overload method (COM) (van der Meer et al., 2011), which is commonly used in Dutch practice to estimate the erosion resistance of grass covers on landward slopes.

The COM is defined in Eq. (11) and can be used to assess erosion damage at any chosen location on the crest or landward slope. The COM computes a damage number D based on the cumulative exceedance of the critical shear stress by N_{ow} overtopping waves.

$$D = \sum_{i=0}^{N_{ow}} \left[(\alpha_a u_i)^2 - {u_c}^2 \right] \tag{11}$$

Here, u_i is the peak flow velocity u_{peak} at the waterside crest line of the ith overtopping wave, α_a is an acceleration factor and basically the ratio between u_{peak} at the assessed location and u_{peak} at the waterside crest line ($= u_{peak}(s)/u_{peak}(0)$). u_c is the critical velocity related to the erosion resistance of the grass cover. Often α_m and α_s are also included in the COM to account for the effects of transitions, however, these are omitted from Eq. (11) for simplicity.

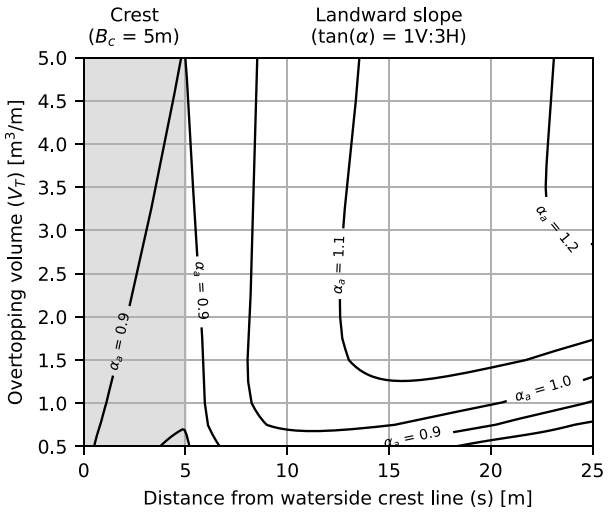

Fig. 17. Acceleration factor α_a, defined as the ratio between the peak flow velocity at location s on the slope and the peak velocity at the waterside crest line for B_c = 5 m, $\tan\alpha$ = 1V:3H, and n = 0.0175.

The COM can be applied at any location along the crest and landward slope, but is often used at the toe of the dike, where the flow velocity has accelerated the most (high α_a) and geometric transitions that increase the loading and weaken the grass cover. Traditionally, for the toe, α_a is set to 1.4 as a first estimate (van der Meer et al., 2014). With our numerical model, a more accurate value of α_a can be obtained based on the calculated flow acceleration.

Fig. 17 shows α_a calculated along a 5-meter-wide crest and a 20-meter-long 1:3 slope for various overtopping volumes. The maximum α_a is approximately 1.25, which is lower than the commonly assumed value of 1.4, which equals a 25% reduction in shear stress since $\tau \propto (\alpha_a u_i)^2$. This difference is caused by the fact that the original derivation of $\alpha_a = 1.4$ neglects the influence of the crest. In our model, α_a at the landward crest line is about 0.9. If the crest is excluded, the resulting α_a increases to approximately 1.4 (1.25/0.9), consistent with van der Meer et al. (2014). This demonstrates that including the crest in the analysis may lead to lower estimates of hydraulic loading than are currently used.

Additionally, we find that α_a increases with overtopping volume. For systems where large overtopping volumes are unlikely (e.g., in upper river reaches), α_a can be adjusted downward based on further analysis. For example, if $V_{T;max}$ = 2.5 m^3/m, an α_a of 1.15 may be more appropriate than 1.25 based on Fig. 17.

As demonstrated in the example, the results of this study provide dike engineers with improved insight into the hydraulic loading exerted by overtopping waves on the crest and landward slope. The influence of design choices such as crest width and slope angle on this loading is thereby better understood. Using the SSSWE-based model, these effects can be quantified and used to better estimate hydraulic loading in existing erosion models, improving their application without replacing them. The model is particularly suitable for parametric studies to quickly assess the effects of different dike geometries due to its computational efficiency. Moreover, the model has the potential to be further extended and validated for more complex geometries, such as landward berms, changes in roughness, and abrupt height transitions, which are not captured by simpler methods.

6. Conclusion

At dikes, overtopping waves generate supercritical transient flow along the crest and landward slope. Understanding the spatial and temporal behavior of this flow is essential for accurate erosion modeling.

This study investigated the spatiotemporal evolution of overtopping flow along dike crests and slopes using a new, efficient numerical model based on the Steep-Slope Shallow Water Equations.

Along the crest, the overtopping flow stretches in time because the local flow velocity near the wavefront is higher than in the tail. Consequently, the peak flow thickness h_{peak} decreases exponentially, while the overtopping time T_{ovt} increases. The peak flow velocity, u_{peak}, decreases only slightly, as the flow momentum remains large relative to friction. As the flow progresses over the crest, the wavefront steepens as h_{peak} shifts toward the wavefront (near u_{peak}), due to local differences in momentum and friction.

Along the landward slope, the flow accelerates due to gravitational forcing, accelerating the flow and increasing u_{peak}. This increases the velocity difference between the wavefront and the tail, stretching the flow further in time. This results in h_{peak} to decrease further due to mass conservation. As the flow becomes faster and thinner downslope, the frictional forcing grows and eventually balances gravitational forcing, causing u_{peak} to decelerate and even reduce, a behavior not captured by current analytical models but observed in field experiments. Larger overtopping volumes require longer slopes to reach this balance. Wavefront steepening continues if u_{peak} and h_{peak} have not fully converged on the crest.

Sensitivity analysis shows that slope angle and surface roughness strongly influence these dynamics. Steeper slopes increase gravitational forcing, yielding higher u_{peak} and shorter T_{ovt}, while shallower slopes reduce acceleration and slightly lengthen T_{ovt}. Rougher surfaces increase friction, reducing u_{peak} and causing slightly less decay of h_{peak}, while smoother surfaces allow higher velocities and more flow stretching. Overall, overtopping flow dynamics are strongly influenced by overtopping volume, crest width, slope angle, and surface roughness.

The results from the numerical model align well with previous studies and provide additional insights by resolving time-dependent dynamics that are not captured by time-independent analytical models. For example, flow stretching, wavefront steepening, a larger decrease in h_{peak} due to the absence of a continuous discharge assumption, and the deceleration and decrease in u_{peak} on long slopes. Moreover, the model is computationally efficient (typically under 10 s), offering a practical middle ground between simplified analytical approaches and full CFD simulations. The schematization used at the upstream boundary at the waterside crest line could be improved by measuring and analyzing natural large-scale measurements of wave overtopping events.

CRediT authorship contribution statement

Niels van der Vegt: Writing – review & editing, Writing – original draft, Visualization, Project administration, Methodology, Investigation, Formal analysis, Conceptualization. **Bas Hofland:** Writing – review & editing, Supervision, Methodology, Funding acquisition, Conceptualization. **Vera M. van Bergeijk:** Writing – review & editing, Methodology, Conceptualization. **Suzanne J.M.H. Hulscher:** Writing – review & editing, Supervision, Methodology, Funding acquisition, Conceptualization. **Jord J. Warmink:** Writing – review & editing, Supervision, Methodology, Funding acquisition, Conceptualization.

Declaration of competing interest

The authors declare that they have no known competing financial interests or personal relationships that could have appeared to influence the work reported in this paper.

Acknowledgments

The authors would like to thank Infram Hydren for providing data on the wave overtopping experiments at Tholen, Millingen a/d Rijn, and Nijmegen (Future Dikes), as well as Dr. Steven A. Hughes for sharing the FlowDike dataset and his analysis of individual overtopping events. This work is part of the Perspectief research programme Future Flood Risk Management Technologies for Rivers and Coasts with project number P21-23. This programme is financed by Domain Applied and Engineering Sciences of the Dutch Research Council (NWO).

Appendix A. List of symbols

Symbol	Description
α	Landward slope angle [rad]
α_a	Acceleration factor of overtopping flow in COM [–]
α_w	Waterside slope angle [rad]
B_c	Crest width [m]
c_d	Gradient of wave run-up thickness (= 0.055) [–]
$c_{h,2\%}$	Coefficient to determine $h_{peak,2\%}$ [–]
$c_{u,2\%}$	Coefficient to determine $u_{peak,2\%}$ [–]
f_v	Shape factor (= 2) [–]
g	Gravitational acceleration constant (= 9.81) [m/s^2]
h	Local flow thickness perpendicular to the slope [m]
h_0	Local flow thickness at the waterside crest line [m]
h_{peak}	Peak flow thickness [m]
$h_{peak,0}$	Peak flow thickness at the waterside crest line [m]
$h_{peak,2\%}$	Peak flow thickness exceeded by 2% of N [m]
h_z	Local flow thickness following cartesian coordinates [m]
H_{m0}	Significant wave height from spectral analysis [m]
H_s	Significant wave height [m]
n	Manning's coefficient [s/m$^{1/3}$]
N	Number of incoming waves [–]
N_{ow}	Number of overtopping waves [–]
q	Local flow discharge [m^2/s]
q_0	Local flow discharge at the wterside crest line [m^2/s]
q_{peak}	Peak flow discharge [m^2/s]
R_c	Freeboard [m]
R_u	Individual wave run-up height [m]
$R_{u,2\%}$	Individual wave run-up height exceeded by 2% of N [m]
s	Distance from waterside crest line or upstream boundary condition [m]
t	Time [s]
t_{front}	Wavefront arrival time [s]
$t_{h_{peak,0}}$	Time lag between wavefront and h_{peak} [s]
$t_{u_{peak,0}}$	Time lag between wavefront and u_{peak} [s]
T_{ovt}	Overtopping time [s]
u	Local flow velocity [m/s]

u_0	Local flow velocity at the waterside crest line [m/s]
u_{bot}	Flow velocity measured just above the bed [m/s]
u_c	Critical flow velocity in COM [m/s]
u_{peak}	Peak flow velocity [m/s]
$u_{peak,0}$	Peak flow velocity at the waterside crest line [m/s]
$u_{peak,2\%}$	Peak flow velocity exceeded by 2% of N [m/s]
u_{top}	Flow velocity measured at the free surface [m/s]
V_T	Individual overtopping volume [m^3/m]
x	Horizontal coordinate [m]

Appendix B. Equations for peak flow characteristics at the waterside crest line

B.1. Equations based on the wave run-up exceedance height

The 2% exceedance values of the peak flow velocity ($u_{peak,2\%,0}$) and peak flow thickness ($h_{peak,2\%,0}$) at the waterside crest line is given by Eq. (12). With the corresponding $c_{u,2\%}$, $b_{u,2\%}$, $c_{h,2\%}$, and $b_{h,2\%}$ coefficients given in Table B.1. The coefficients $b_{u,2\%}$ and $b_{h,2\%}$ are only used in the equations proposed by Formentin et al. (2019), for other models, these coefficients are 1.0.

Under the assumption that run-up and peak flow characteristics both follow Rayleigh distributions (Battjes, 1974; van der Meer et al., 2012; van Damme, 2016), the coefficients are applied to individual run-up events within this study: $c_{u,2\%} = c_u$ and $c_{h,2\%} = c_h$.

$$\begin{aligned} u_{peak,2\%,0} &= c_{u,2\%}\sqrt{g\left(R_{u,2\%} - R_c\right)}^{b_{u,2\%}} \\ h_{peak,2\%,0} &= c_{h,2\%}\left(R_{u,2\%} - R_c\right)^{b_{h,2\%}} \end{aligned} \tag{12}$$

B.2. Equations based on individual overtopping volume

The equations relating the individual overtopping volume (V_T) to the peak flow velocity ($u_{peak,0}$) and peak flow thickness ($h_{peak,0}$) at the waterside crest line are derived from individual overtopping events.

The equations by van der Meer et al. (2011) are given in Eq. (13). It should be noted that these equations are derived specifically from the flow from the wave overtopping simulator.

$$\begin{aligned} u_{peak,0} &= 5.0\,{V_T}^{0.34} \\ h_{peak,0} &= 0.133\,{V_T}^{0.5} \end{aligned} \tag{13}$$

The equations by Hughes (2017) are given in Eq. (14).

$$\begin{aligned} u_{peak,0} &= 27.67\frac{\sqrt{V_T\,\tan(\alpha_w)}}{T_{m-1,0}} \\ h_{peak,0} &= 0.324\,{V_T}^{0.5} \end{aligned} \tag{14}$$

Appendix C. Validation with field experiments

C.1. Schematization

To validate the numerical model, we use measurements from three field experiments conducted with the Wave Overtopping Simulator (WOS): Tholen, Millingen a/d Rijn, and Nijmegen (Future Dikes). These cases together provide a dataset of 89 individual overtopping volumes, ranging from 0.1 to 5.5 m^3/m.

Figs. 18, 19, and 20 show the geometry of the three cases based on field surveys by Infram (Bakker et al., 2011, 2013; Daamen et al., 2023) (black line) and schematized in the numerical model (red dashed line). As discussed in Section 3.2, the computational domain starts at the first measurement location where both the flow velocity and flow thickness are measured, which lies on the crest in all cases. van Bergeijk et al. (2020) estimated a Manning's coefficient of $n = 0.0175$ for (part of) these experiments. We apply this value to the entire surface, as the computational domain is fully grass-covered.

In each figure, markers indicate the measurement locations and the type of instrument used. Surfboards are equipped with integrated paddle-wheels, yielding measurements of both the flow thickness h and the surface velocity u_{top}. Locations with only paddle-wheels measure the flow velocity near the bottom of the overtopping flow, u_{bot}, with the sensors mounted just above the ground.

C.2. Boundary conditions

Since the overtopping flow is generated by the WOS, the boundary conditions from Section 2 cannot be applied directly. To account for the different flow characteristics, the upstream boundary is placed at the first measurement location. Then, the relationships between the individual overtopping volume V_T and the peak flow velocity u_{peak}, peak flow thickness h_{peak}, and overtopping duration T_{ovt} at this boundary are derived from on measurements. This ensures that any differences between model and measurements result from flow propagation, rather than from inconsistencies between the WOS-generated flow and the schematization of real overtopping conditions.

To define these specific relationships for these cases, we first need to obtain u_{peak}, h_{peak}, and T_{ovt} from the measurements at this location. First, u_{peak} and h_{peak} follow from the maxima of their measurements. Next, the overtopping duration is determined from the flow thickness measurement, as it provides a smoother signal in the tail of the overtopping event. Specifically, T_{ovt} is defined as the period during which the flow thickness exceeds 2 cm. This threshold is manually verified and adjusted if necessary for each case.

Since previous studies have shown that the relationships between V_T and u_{peak}, h_{peak}, and T_{ovt} can be described by power laws (van der Meer et al., 2011; Hughes, 2017), we apply the same approach here. New power-law relations are fitted, see Fig. 21. When simulating the overtopping flow for each case, we replace the generalized relations from Section 2 with fitted, case-specific relations to better represent the WOS-generated flow. These relations are calibrated solely for the three validation cases at the first measurement location and are not applicable beyond this context.

C.3. Temporal evolutions of outliers

See Figs. 22 and 23 for the outliers discussed in Section 3.2.

Table B.1
Different values for c_h, b_h, c_u and b_u by different studies.

Study	$c_{u,2\%}$	$b_{u,2\%}$	$c_{h,2\%}$	$b_{h,2\%}$	Range
van Gent (2002)	1.30	1.0	0.15	1.0	1:2.5–1:4
Schüttrumpf and Oumeraci (2005)	1.37	1.0	0.33	1.0	1:4–1:6
Bosman et al. (2009)	$0.30/\sin\alpha_w$	1.0	$0.01/\sin^2\alpha_w$	1.0	1:4–1:6
van der Meer et al. (2011)	$0.35\cot\alpha_w$	1.0	0.13	1.0	1:3–1:6
van der Meer et al. (2012)/EurOtop (2018)	1.4–1.5	1.0	0.2–0.3	1.0	1:3–1:6
Formentin et al. (2019)	$0.12\cot\alpha_w$+0.41	1.35	$0.085\cot\alpha_w$	1.35	1:2–1:6

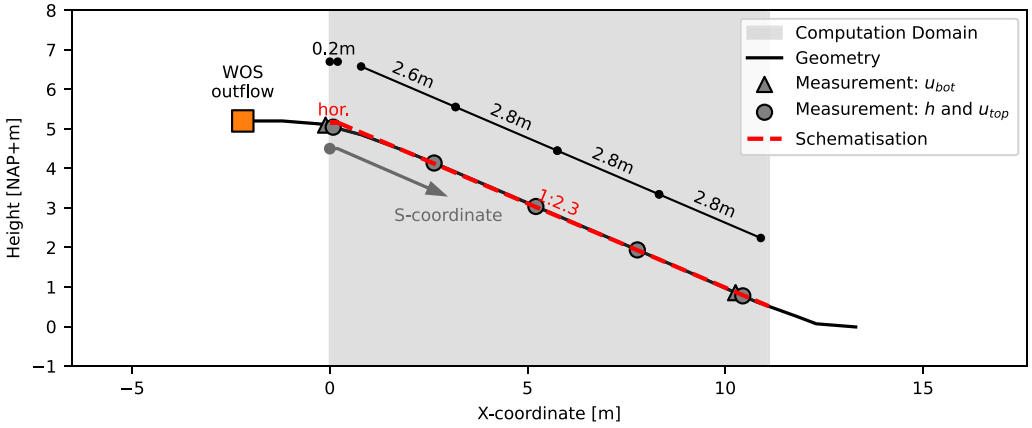

Fig. 18. Geometry of Tholen from field surveys (black line) (Bakker et al., 2011) and as schematized in the model (red dashed line). The computational domain is shown in gray hatching. Markers indicate measurement locations and types.

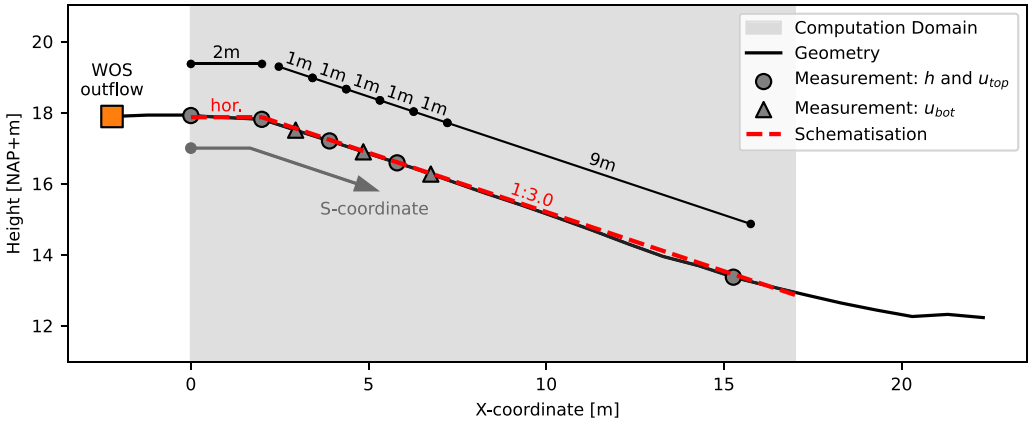

Fig. 19. Geometry of Millingen a/d Rijn from field surveys (black line) (Bakker et al., 2013) and as schematized in the model (red dashed line). The computational domain is shown in gray hatching. Markers indicate measurement locations and types.

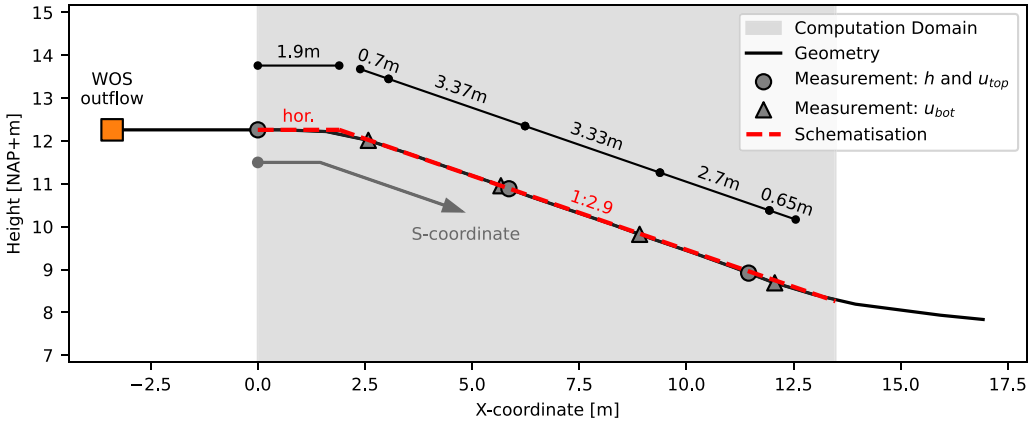

Fig. 20. Geometry of Nijmegen (Future Dikes) from field surveys (black line) (Daamen et al., 2023) and as schematized in the model (red dashed line). The computational domain is shown in gray hatching. Markers indicate measurement locations and types.

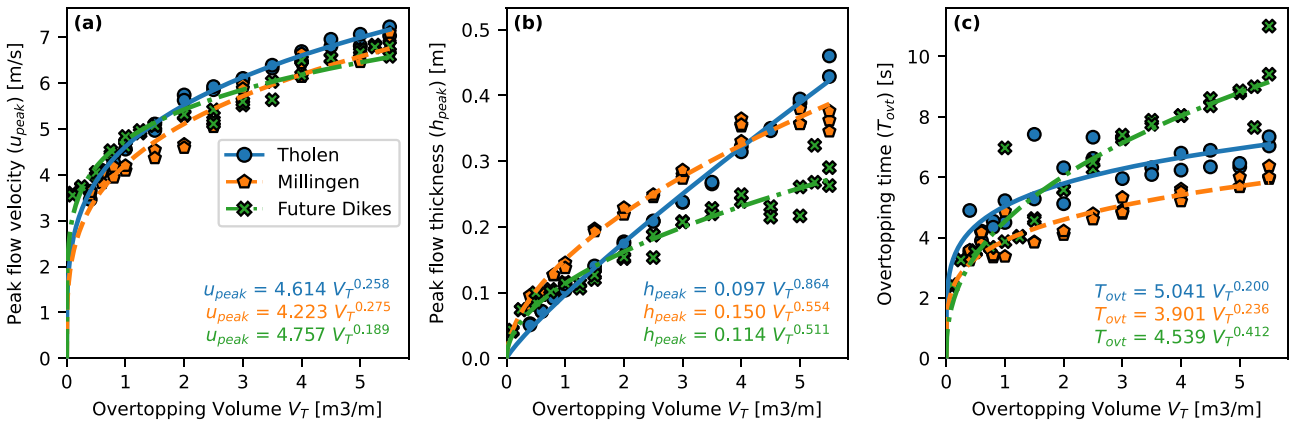

Fig. 21. Relationships between the individual overtopping volume V_T and overtopping flow characteristics at the first measurement location for three different cases: (a) peak flow velocity u_{peak}; (b) peak flow thickness h_{peak}; (c) overtopping time T_{ovt}. The different cases are indicated by color.

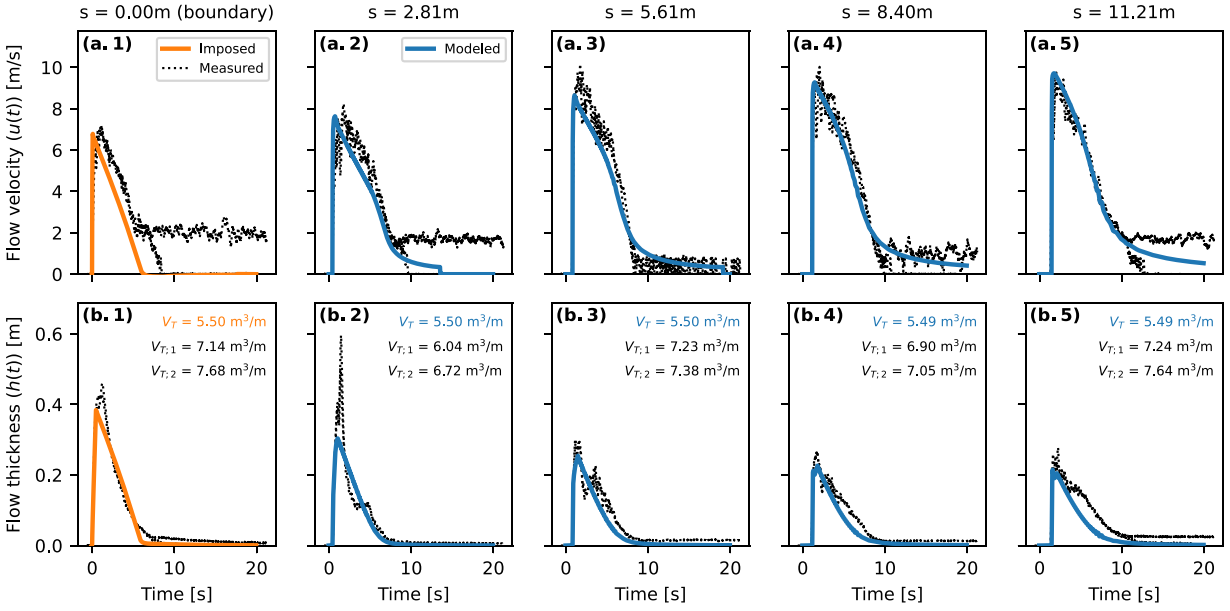

Fig. 22. Comparison between measured and modeled overtopping flow for an overtopping wave with V_T = 5.5 m^3/m at Tholen. Top row (a.1–a.5): flow velocity $u(t)$; bottom row (b.1–b.5): flow thickness $h(t)$. Individual measurements are indicated with superscript numbers. Columns correspond to increasing distance s along the crest and landward slope (s = 0, 2.81, 5.61, 8.40, and 11.21 m). In Figure b.2, the peak flow thickness is dominated by an (unrealistic) sharp peak compared to the other locations.

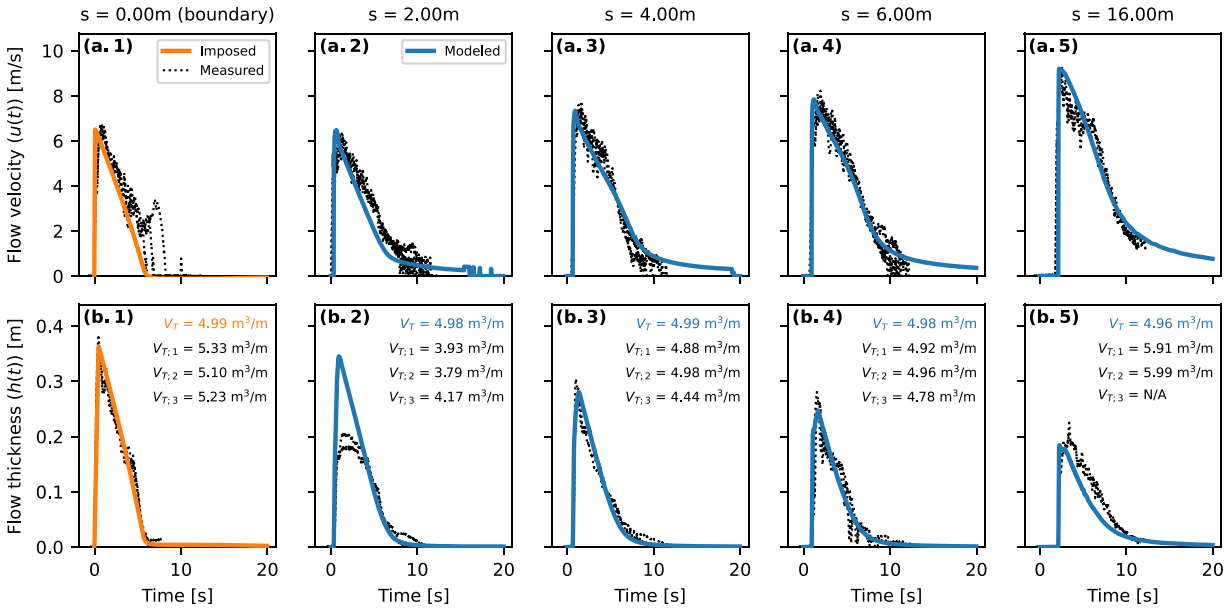

Fig. 23. Comparison between measured and modeled overtopping flow for an overtopping wave with V_T = 5.0 m³/m at Millingen a/d Rijn. Individual measurements are indicated with superscript numbers. Top row (a.1–a.5): flow velocity $u(t)$; bottom row (b.1–b.5): flow thickness $h(t)$. Columns correspond to increasing distance s along the crest and landward slope (s = 0, 2, 4, 6, and 16 m). In Figure b.2, the peak flow thickness appears truncated compared to the other locations.

Data availability

The developed numerical model is available as a Python package via PyPi under the name *boreflow* (van der Vegt, 2025). The source code, including examples are available on GitHub under the GPL-3.0 license: https://github.com/nielsvandervegt/boreflow.

References

Altomare, C., Gironella, X., Crespo, A.J.C., 2021. Simulation of random wave overtopping by a WCSPH model. Appl. Ocean Res. 116, 102888. http://dx.doi.org/10.1016/j.apor.2021.102888.

Ancey, C., Iverson, R.M., Rentschler, M., Denlinger, R.P., 2008. An exact solution for ideal dam-break floods on steep slopes. Water Resour. Res. 44 (1), http://dx.doi.org/10.1029/2007wr006353.

Audusse, E., Bouchut, F., Bristeau, M.O., Klein, R., Perthame, B., 2004. A fast and stable well-balanced scheme with hydrostatic reconstruction for shallow water flows. SIAM J. Sci. Comput. 25 (6), 2050–2065. http://dx.doi.org/10.1137/s1064827503431090.

Bakker, J., Melis, R., Mom, R.J.C., 2013. Factual Report: Overslagproeven Rivierenland (Dutch) [Factual Report: Wave Overtopping Experiments Waterboard Rivierenland]. Technical Report 12i071, Infram, Marknesse, p. 105.

Bakker, J.J., Mom, R.J.C., Steendam, G.J., Van der Meer, J.W., 2011. Factual Report. Overslagproeven en oploopproef Tholen (Dutch) [Factual Report. Wave overtopping en runup experiments Tholen]. Technical Report 10i092, Infram.

Battjes, J.A., 1974. Computation of Set-Up, Longshore Currents, Run-Up and Overtopping Due to Wind-Generated Waves (Ph.D. thesis). Delft University of Technology, Delft, URL http://resolver.tudelft.nl/uuid:e126e043-a858-4e58-b4c7-8a7bc5be1a44.

Bosman, G., van der Meer, J., Hoffmans, G., Schüttrumpf, H., Verhagen, H., 2009. Individual overtopping events at dikes. In: Coastal Engineering 2008 - Conference Proceedings. World Scientific Publishing Company, pp. 2944–2956. http://dx.doi.org/10.1142/9789814277426_0244.

Chen, W., Warmink, J.J., van Gent, M.R.A., Hulscher, S.J.M.H., 2021. Numerical modelling of wave overtopping at dikes using openfoam®. Coast. Eng. 166, 103890. http://dx.doi.org/10.1016/j.coastaleng.2021.103890.

Chen, W., Warmink, J.J., van Gent, M.R.A., Hulscher, S.J.M.H., 2022. Numerical investigation of the effects of roughness, a berm and oblique waves on wave overtopping processes at dikes. Appl. Ocean Res. 118, 102971. http://dx.doi.org/10.1016/j.apor.2021.102971.

Chow, V.T., 2009. Open-Channel Hydraulics. Blackburn Press, West Caldwell, NJ, ISBN-13: 978-1932846188.

Courant, R., Friedrichs, K., Lewy, H., 1928. Über die partiellen differenzengleichungen der mathematischen physik (German) [on the partial difference equations of mathematical physics]. Math. Ann. 100 (1), 32–74. http://dx.doi.org/10.1007/bf01448839.

Daamen, E., Heida, L., Mom, R.J.C., Overduin, M., Wauben, C., 2023. Factual Report. Praktijkproeven Future Dikes (Dutch) [Factual report. Field Experiments Future Dikes]. Technical Report 21i873, Infram, v2.0.

Dean, R.G., Rosati, J.D., Walton, T.L., Edge, B.L., 2010. Erosional equivalences of levees: Steady and intermittent wave overtopping. Ocean Eng. 37 (1), 104–113. http://dx.doi.org/10.1016/j.oceaneng.2009.07.016.

Delis, A.I., 2002. Improved application of the HLLE Riemann solver for the shallow water equations with source terms. Commun. Numer. Methods Eng. 19 (1), 59–83. http://dx.doi.org/10.1002/cnm.570.

EurOtop, 2018. Manual on Wave Overtopping of Sea Defences and Related Structures. An Overtopping Manual Largely Based on European Research, but for Worldwide Application. Technical Report, EurOtop, van der Meer J.W., Allsop N.W.H., Bruce, T., De Rouck J., Kortenhaus A., Pullen T., Schüttrumpf H., Troch P., and Zanuttigh B., www.overtopping-manual.com.

Formentin, S., Gaeta, M., Palma, G., Zanuttigh, B., Guerrero, M., 2019. Flow depths and velocities across a smooth dike crest. Water 11 (10), 2197. http://dx.doi.org/10.3390/w11102197.

Gruwez, V., Altomare, C., Suzuki, T., Streicher, M., Cappietti, L., Kortenhaus, A., Troch, P., 2020. Validation of RANS modelling for wave interactions with sea dikes on shallow foreshores using a large-scale experimental dataset. J. Mar. Sci. Eng. 8 (9), 650. http://dx.doi.org/10.3390/jmse8090650.

Guo, X., Wang, B., Liu, H., Miao, G., 2014. Numerical simulation of two-dimensional regular wave overtopping flows over the crest of a trapezoidal smooth impermeable sea dike. J. Waterw. Port Coast. Ocean. Eng. 140 (3), http://dx.doi.org/10.1061/(asce)ww.1943-5460.0000234.

Harten, A., Lax, P.D., van Leer, B., 1983. On upstream differencing and Godunov-type schemes for hyperbolic conservation laws. SIAM Rev. 25 (1), 35–61. http://dx.doi.org/10.1137/1025002.

Heller, V., 2011. Scale effects in physical hydraulic engineering models. J. Hydraul. Res. 49 (3), 293–306. http://dx.doi.org/10.1080/00221686.2011.578914.

Hofland, B., Diamantidou, E., van Steeg, P., Meys, P., 2015. Wave runup and wave overtopping measurements using a laser scanner. Coast. Eng. 106, 20–29. http://dx.doi.org/10.1016/j.coastaleng.2015.09.003.

Hughes, S.A., 2015. Hydraulic Parameters of Individual Overtopping Wave Volumes. Technical Report, Colorado State University - Engineering Research Center, Fort Collins, CO, p. 68.

Hughes, S.A., 2017. Hydraulic parameters of overtopping wave volumes. In: Coastal Structures and Solutions To Coastal Disasters 2015 - Conference Proceedings. American Society of Civil Engineers, pp. 710–718. http://dx.doi.org/10.1061/9780784480304.075.

Hughes, S.A., Shaw, J.M., 2011. Continuity of instantaneous wave overtopping discharge with application to stream power concepts. J. Waterw. Port Coast. Ocean. Eng. 137 (1), 12–25. http://dx.doi.org/10.1061/(ASCE)WW.1943-5460.0000057.

Hughes, S.A., Thornton, C.I., 2016. Estimation of time-varying discharge and cumulative volume in individual overtopping waves. Coast. Eng. 117, 191–204. http://dx.doi.org/10.1016/j.coastaleng.2016.08.006.

Hughes, S.A., Thornton, C.I., van der Meer, J.W., Scholl, B.N., 2012. Improvements in describing wave overtopping processes. In: Coastal Engineering 2012 - Conference Proceedings, vol. 3, Coastal Engineering Research Council, pp. 2085–2099. http://dx.doi.org/10.9753/icce.v33.waves.35.

Ibrahim, M.S.I., Baldock, T.E., 2021. Physical and numerical modeling of wave-by-wave overtopping along a truncated plane beach. J. Waterw. Port Coast. Ocean. Eng. 147 (5), http://dx.doi.org/10.1061/(asce)ww.1943-5460.0000663.

Jasak, H., 2009. OpenFOAM: Open source CFD in research and industry. Int. J. Nav. Archit. Ocean. Eng. 1 (2), 89–94. http://dx.doi.org/10.2478/ijnaoe-2013-0011.

Lorke, S., Bornschein, A., Schüttrumpf, H., Pohl, R., 2012. FlowDike-D. Influence of Wind and Current on Wave Run-Up and Wave Overtopping. Technical Report, RWTH Aachen and TU Dresden, URL http://resolver.tudelft.nl/uuid:73cb6cbe-8931-4499-b4d6-aa31548f5dda.

Manning, R., 1891. On the flow of water in open channels and pipes. Trans. Inst. Civ. Eng. Irel. 20 (1), 161–207.

Maranzoni, A., Tomirotti, M., 2022. New formulation of the two-dimensional steep-slope shallow water equations. Part I: Theory and analysis. Adv. Water Resour. 166, 104255. http://dx.doi.org/10.1016/j.advwatres.2022.104255.

Nash, J.E., Sutcliffe, J.V., 1970. River flow forecasting through conceptual models part I — A discussion of principles. J. Hydrol. 10 (3), 282–290. http://dx.doi.org/10.1016/0022-1694(70)90255-6.

Ponsioen, L., van Damme, M., Hofland, B., Peeters, P., 2019. Relating grass failure on the landside slope to wave overtopping induced excess normal stresses. Coast. Eng. 148, 49–56. http://dx.doi.org/10.1016/j.coastaleng.2018.12.009.

Roe, P.L., 1986. Characteristic-based schemes for the Euler equations. Annu. Rev. Fluid Mech. 18 (1), 337–365. http://dx.doi.org/10.1146/annurev.fl.18.010186.002005.

Runge, C., 1895. Ueber die numerische Auflösung von Differentialgleichungen [German] (On the numerical solution of differential equations). Math. Ann. 46 (2), 167–178. http://dx.doi.org/10.1007/bf01446807.

Rusanov, V.V., 1961. Calculation of intersection of non-steady shock waves with obstacles. J. Comput. Math. Math. Phys. 1, 267–279.

Schrama, W.P., van Bergeijk, V.M., Mares-Nasarre, P., den Bieman, J.P., van Gent, M.R.A., Aguilar-López, J.P., 2026. Surrogate modelling of dike wave overtopping hydrodynamics using an adapted deep learning vision transformer. Coast. Eng. 203, 104874. http://dx.doi.org/10.1016/j.coastaleng.2025.104874.

Schüttrumpf, H., Oumeraci, H., 2005. Layer thicknesses and velocities of wave overtopping flow at seadikes. Coast. Eng. 52 (6), 473–495. http://dx.doi.org/10.1016/j.coastaleng.2005.02.002.

Schüttrumpf, H., van Gent, M.R.A., 2003. Wave overtopping at seadikes. In: Coastal Structures 2003 - Conf. Proc.. American Society of Civil Engineers, pp. 431–443. http://dx.doi.org/10.1061/40733(147)36.

Smith, G.M., 1994. Grasdijken: Graserosie, reststerkte en golfoverslag (Dutch) [Grass dikes: Grass erosion, residual strength and wave overtopping]. Technical Report H1565, Delft Hydraulics, URL http://resolver.tudelft.nl/uuid:113e4233-0cc8-439f-b0fd-5baa30569d83.

Suzuki, T., Altomare, C., Veale, W., Verwaest, T., Trouw, K., Troch, P., Zijlema, M., 2017. Efficient and robust wave overtopping estimation for impermeable coastal structures in shallow foreshores using SWASH. Coast. Eng. 122, 108–123. http://dx.doi.org/10.1016/j.coastaleng.2017.01.009.

Toro, E.F., 2009. Riemann Solvers and Numerical Methods for Fluid Dynamics: A Practical Introduction. Springer Berlin Heidelberg, http://dx.doi.org/10.1007/b79761, ISBN-13: 978-3540498346.

van Bergeijk, V.M., Verdonk, V.A., Warmink, J.J., Hulscher, S.J.M.H., 2021. The cross-dike failure probability by wave overtopping over grass-covered and damaged dikes. Water 13 (5), 690. http://dx.doi.org/10.3390/w13050690.

van Bergeijk, V.M., Warmink, J.J., Hulscher, S.J.M.H., 2020. Modelling the wave overtopping flow over the crest and the landward slope of grass-covered flood defences. J. Mar. Sci. Eng. 8 (7), 489. http://dx.doi.org/10.3390/jmse8070489.

van Bergeijk, V.M., Warmink, J.J., Hulscher, S.J.M.H., 2022. The wave overtopping load on landward slopes of grass-covered flood defences: Deriving practical formulations using a numerical model. Coast. Eng. 171, 104047. http://dx.doi.org/10.1016/j.coastaleng.2021.104047.

van Bergeijk, V.M., Warmink, J.J., van Gent, M.R.A., Hulscher, S.J.M.H., 2019. An analytical model of wave overtopping flow velocities on dike crests and landward slopes. Coast. Eng. 149, 28–38. http://dx.doi.org/10.1016/j.coastaleng.2019.03.001.

van Damme, M., 2016. Distributions for wave overtopping parameters for stress strength analyses on flood embankments. Coast. Eng. 116, 195–206. http://dx.doi.org/10.1016/j.coastaleng.2016.06.010.

van der Meer, J.W., 2007. Design, Construction, Calibration and Use of the Wave Overtopping Simulator. Technical Report 04i103, Infram, V3.3. http://resolver.tudelft.nl/uuid:5656bf8b-e799-4c7f-87d4-82d4f8a26fef.

van der Meer, J., Hardeman, B., Steendam, G., Schüttrumpf, H., Verheij, H., 2011. Flow depths and velocities at crest and landward slope of a dike, in theory and with the wave overtopping simulator. In: Coastal Engineering 2010 - Conference Proceedings, vol. 4, Coastal Engineering Research Council, pp. 2728–2742. http://dx.doi.org/10.9753/icce.v32.structures.10.

van der Meer, J.W., Hoffmans, G., van Hoven, A., 2014. Analyses grass erosion in wave run-up and wave overtopping conditions. Technical Report 1209437-005-HYE-0003, van der Meer Consulting and Deltares, URL https://resolver.tudelft.nl/uuid:05d5a9c0-5281-4ff1-8ab7-64645ed1bc93.

van der Meer, J., Klein Breteler, M., 1991. Measurement and computation of wave induced velocities on a smooth slope. In: Coastal Engineering 1990 - Conference Proceedings, vol. 113, American Society of Civil Engineers, pp. 191–204. http://dx.doi.org/10.1061/9780872627765.016.

van der Meer, J.W., Provoost, Y., Steendam, G.J., 2012. The wave run-up simulator, theory and first pilot test. In: Coastal Engineering 2012 - Conference Proceedings, vol. 5, Coastal Engineering Research Council, pp. 4069–4083. http://dx.doi.org/10.9753/icce.v33.structures.65.

van der Meer, J.W., Steendam, G.J., Mosca, C.A., Guzzo, L.B., Takata, K., Cheong, N.S., Eng, C.K., LJ, L.A., Ling, G.P., Siang, C.W., Seng, C.W., Karthikeyan, M., SC, F.Y., Govindasamy, V., 2020. Wave overtopping tests to determine tropical grass species and topsoils for polder dikes in a tropical country. Coast. Eng. Proc. (36v), 338–352. http://dx.doi.org/10.9753/icce.v36v.papers.31.

van der Vegt, N., 2025. BoreFlow v0.1.3. URL https://github.com/nielsvandervegt/boreflow.

van der Vegt, N., Warmink, J.J., Hofland, B., van Bergeijk, V.M., Hulscher, S.J.M.H., 2025. Variation in flow characteristics of overtopping waves on dike crests. Coast. Eng. 201, 104772. http://dx.doi.org/10.1016/j.coastaleng.2025.104772.

van Gent, M.R.A., 2002. Low-Exceedance Wave Overtopping Events: Measurements of Velocities and the Thickness of Water-Layers on the Crest and Inner Slope of Dikes. Technical Report DC030202/H3803, Delft Cluster, URL http://resolver.tudelft.nl/uuid:e71289dd-f6aa-471e-856c-832071a83753.

van Hoven, A., Verheij, H., Hoffmans, G., van der Meer, J.W., 2013. Evaluation and Model Development. Grass Erosion Test at the Rhine dike. Technical Report 1207811-002-HYE-0007-svb, Deltares, p. 137.

van Leer, B., 1974. Towards the ultimate conservative difference scheme. II. Monotonicity and conservation combined in a second-order scheme. J. Comput. Phys. 14 (4), 361–370. http://dx.doi.org/10.1016/0021-9991(74)90019-9.

van Leer, B., 1977. Towards the ultimate conservative difference scheme III. upstream-centered finite-difference schemes for ideal compressible flow. J. Comput. Phys. 23 (3), 263–275. http://dx.doi.org/10.1016/0021-9991(77)90094-8.

van Leer, B., 1979. Towards the ultimate conservative difference scheme. V. A second-order sequel to Godunov's method. J. Comput. Phys. 32 (1), 101–136. http://dx.doi.org/10.1016/0021-9991(79)90145-1.

Vuik, C., Vermolen, F.J., van Gijzen, M.B., Vuik, M.J., 2023. Numerical Methods for Ordinary Differential Equations. TU Delft OPEN Publishing, http://dx.doi.org/10.5074/t.2023.001, ISBN-13: 978-9463666657.

Zijlema, M., Stelling, G., Smit, P., 2011. SWASH: An operational public domain code for simulating wave fields and rapidly varied flows in coastal waters. Coast. Eng. 58 (10), 992–1012. http://dx.doi.org/10.1016/j.coastaleng.2011.05.015.